AMPLIFICATION IN A STOCHASTIC TWO DIMENSIONAL MODEL OF EUKARYOTIC GRADIENT SENSING

by

SUPARAT CHUECHOTE

Submitted in partial fulfillment of the requirements

For the degree of Master of Science

Thesis Adviser: Dr. Peter J. Thomas

Department of Mathematics

CASE WESTERN RESERVE UNIVERSITY

August, 2010

CASE WESTERN RESERVE UNIVERSITY

SCHOOL OF GRADUATE STUDIES

We hearby approve the thesis/dissertation of

Miss Suparat Chuechote

candidate for the MS degree*.

(signed) Professor Peter J. Thomas
(chair of the committee)

Professor Erkki Somersalo

Professor Harihara Baskaran

(date) 05/27/2010

*We also certify that written approval has been obtained for any proprietary material contained therein.

Contents

List of Tables

List of Figures

Acknowledgements

I am heartily thankful to my advisor, Professor Peter J. Thomas, and whose encouragement, guidance and support from the initial to the final level enabled me to develop an understanding of the subject. I also sincerely thank my other committee members, Professor Erkki Somersalo, Professor David Gurarie Professor Hari Baskaran, who gives me knowledges and feedbacks from biological aspects. I feel delighted to have been working with my advisor and my colleagues, Wendy Smith, Stephen Fleming and Heather McGinnis. For general support, I thank the department assistant and secretaries, Jeanne Jurkovich, Diane Robinson and Gaythreesa Lewis. Acknowledgements are also made to the Royal Thai Government and the Office of Education Affairs, Royal Thai Embassy in Washington DC, USA. for providing me a full scholarship and great opportunity to study at Case Western Reserve University. Lastly, I offer my regards and blessings to all of those who supported me in any respect during the completion of the project.

This material is based upon work supported in part by the National Science Foundation under Grant No. DMS-0720142. Any opinions, findings, and conclusions or recommendations expressed in this material are those of the author and do not necessarily reflect the views of the National Science Foundation.

List of Abbreviations

S	Activated receptor in the balance inactivation model
A	Activator in the balance inactivation model
B	Cytosolic inhibitor in the balance inactivation model
Bm	Membrane-bound inhibitor
PDGF	Platelet derived growth factor
PMN	Polymorphonuclear neutrophil leukocyte
cAMP	Adenosine (3',5') -cyclic monophosphate
GC	Guanylyl cyclase
PI3K	Phosphoinositide 3-kinase
PTEN	PI 3-phosphatase
cGMP	Guanosine (3',5')-cyclic monnophosphate
PH	Pleckstrin Homology
LEGI	Local excitation and global inhibition
CME	Chemical master equation
SSA	Stochastic simulation algorithm
MSA	Multinomial simulation algorithm
GFEM	Galerkin finite element method
D	Diffusion coefficient
Q	Markov transition matrix
ε	Fractional gradient
Θ	True gradient direction

Amplification in a Stochastic Two Dimensional Model
of Eukaryotic Gradient Sensing

Abstract

by

SUPARAT CHUECHOTE

Chemotaxis is the directed migration of cells guided by chemical gradients. Chemotaxis combine sseveral biological mechanisms, the first of which is gradient sensing. The accuracy with which a cell can determine the direction of an external chemical gradient is limited by fluctuations arising from the discrete nature of second messenger release and diffusion processes within the small volume of a living cell. We implement a stochastic version a Balanced Inactivation gradient sensing model introduced by (Levine *et al.* 2006) in a two dimensional geometry. We develop a fixed timestep approach in which the probabilities of individual molecules making chemical transitions is handled as a system of multinomial random variables. With this numerical platform we investigate the relationship between the amplification of the gradient signal, nonlinear saturation at large gradients, and fundamental limits on the accuracy of the gradient sensing mechanism.

1 Introduction

1.1 Gradient Sensing and Chemotaxis

Chemotaxis is the directed migration of cells guided by chemical gradients. It is an essential mechanism in many biological processes. For example, fibroblasts move toward a platelet derived growth factor (PDGF) during the wound healing process; cellular organization during embryogenesis occurs by response of cells to chemotactic stimuli; polymorphonuclear neutrophil leukocytes (PMNs) are directed to sites of inflammation in the immune system; and a *Dictyostelium discoideum* amoeba uses chemotaxis to find its food source and aggregate with conspecific cells during periods of starvation [4, 24, 29]. During chemotaxis, extracellular signals are translated into complex cellular responses such as changes in morphology and motility. This mechanism is induced by various cellular signaling networks. To understand the chemotaxis mechanism at a molecular level, it is crucial to obtain detailed information about the localization and dynamics of signaling processes. According to Iglesias and Devreotes, chemotaxis consists of three mechanisms; motility, polarization and gradient sensing [4, 9, 10]. 1) **Motility** is the ability of chemotactic cells to move by periodic extension and retraction of pseudopodia. This process does not require the existence of chemoattractants. 2) **Polarization** occurs when cells arrange their cellular components to differentiate sensitivities for a chemoattractant. The reorganization of cellular components leads to well-defined leading and trailing regions. 3) **Gradient sensing** occurs when a cell is able to detect and amplify spatial gradients [10]. Understanding how these three mechanisms couple to cellular morphology and motility will clarify the biology of cell migration during chemotaxis.

Recent research has highlighted similarities between chemotaxis in mammalian leukocytes (white blood cells) and in the social amoeba *Dictyostelium discoideum* [19]. This organism grows in soil that contains bacteria. With sufficient bacteria as their nutrient, *Dictyostelium* cells live as individual amoebae. Upon depleting their food

supply, they release and respond to adenosine (3',5')-cyclic monophosphate (cAMP) as their signal of starvation, which induces the cells to aggregate. The aggregated cells then transform into a slug and hence a fruiting body. Consequently, spores from the fruiting body are spread to new livable sites and their life cycle restarts. Chemotaxis is essential to *Dictyostelium* in the process of finding bacteria in the vegetative stage and to aggregate in starvation where *Dictyostelium* cells move in response to a concentration gradient cAMP. In comparison, mammalian leukocytes navigate by following extracellular gradients of signaling molecules such as fMLP, a peptide released by bacterial pathogens, or interleukin-8, a distress signal released by damaged host tissue. These chemoattractants play a role for leukocytes analogous to the role of cAMP in *Dictyostelium* aggregation. Both types of cells exploit the G-protein signaling pathways to mediate directional migration [19]. Therefore, *Dictyostelium* is widely used as a model organism for the study of chemotaxis because it has a complete genome profile and biochemical accessibility. The investigation of signaling pathways of *Dictyostelium* can lead to the discoveries of features of pathways in mammalian systems [19].

This study focuses on the gradient sensing mechanism in the aggregation process of *Dictyostelium*. This process necessarily involves the spatial structure of the cell (making zero-dimensional or point models uninteresting for this system). At the unicellular level, the cAMP molecules bind to cAMP receptors (cARs) on the plasma membrane of a *Dictyostelium* cell. The cAMP-bound receptors interact with heterotrimeric guanosine triphosphate (G-proteins) located on the inner face of the plasma membrane. The heterotrimeric G-protein has three subunits, G_α, G_β and G_γ. Upon cAMP binding, the receptor rapidly dissociates its subunits into G_α and $G_{\beta\gamma}$ components which are free to interact with downstream effectors and hence generate cellular signals [13, 19].

Many downstream effectors influence the formation of the leading and trailing edges of a chemotactic cell, including guanylyl cyclase (GC), phosphoinositide 3-

kinase (PI3K) and PI 3-phosphatase (PTEN) [11]. Soluble GC (sGC) plays a role in generating cGMP (guanosine (3',5')-cyclic monophosphate) of the cells. Since the cGMP is responsible for myosin filament formation at the rear of the cell and suppression of pseudopod formation at the lateral edges and back of the cell, cells lacking sGC tend to have low chemotactic activity and aggregate slowly [2]. Furthermore, the PI3K and PTEN are the two effectors that control leading edge activity of a chemotactic cell. They act oppositely to one another. While G-protein influences the activation of PI3K and PTEN, PI3K increases local levels of phosphatidylinositol triphosphate, PI(3,3,5)P_3, at the plasma membrane, while PTEN is responsible for PI(3,4,5)P_3 degradation. The local levels of PI(3,4,5)P_3 at inner cell membrane regulate actin polymerization at the leading edge of the cell by recruiting pleckstrin homology (PH) domain-containing proteins [2, 23]. Therefore, extracellular gradients directly influence the localization of PI(3,4,5)P_3-bound PH domain at the leading edge of the cells and localization of PTEN at the trailing edge.

1.2 Variability in Chemotactic Behavior

The ability of cells to detect extracellular gradients involves multiple catalytic reactions, such as cAMP-receptors binding, interaction of PI(3,4,5)P_3 to PH domain, and binding of PTEN to the plasma membrane. Because interactions among individual molecules fluctuate due to a cell's environment and thermal fluctuation, signaling processes in gradient sensing can become noisy and hence lead to inaccurate gradient detection. In addition, diffusion of second-messenger molecules involved in gradient sensing, such as PTEN and cGMP, causes signal dispersion and spatial gradient information is not fully rendered. The possible reason can be the variation in diffusion rates of the second-messenger molecules due to their size and location [24]. The dynamics of PTEN molecules has been observed by means of internal reflection microscopy, which showed that individual PTEN molecules bind to plasma membrane for only about 300 ms [6, 21]. Furthermore, Miyanaga *et al.* [21] identified the stochastic signal

transduction processes of chemotaxis. They visualized the localization of $PI(3,4,5)P_3$ on the membrane by fluorenscently tagging PH domain-containing protein, Crac, that binds specifically to $PI(3,4,5)P_3$. The Crac-GFP served as a reporter for the cellular response to chemoattractants since the localization of Crac-GFP took place at a high concentration of cAMP and in the direction of pseudopod formation. The result also showed that Crac-GFP localization on the membrane is maintained by the rapid exchange of individual molecules. This result confirmed that the chemotactic signaling process is stable but the underlying reaction is stochastic [21]. Therefore, stochastic noise should be taken into account in order to simulate the gradient sensing mechanism of the eukaryotic cells.

1.3 Amplification in Gradient Sensing Pathways

Eukaryotic cells such as *Dictyostelium* and human neutrophils have a remarkable ability to sense the direction of weak extracellular chemical gradients. Gradients as small as an $\approx 1\%$ difference in receptor occupancy between front and back can produce reliable chemotaxis [31]. This fascinating navigational ability compels us to investigate the transduction mechanism to understand how weakly localized signals convert to strongly localized responses. Postma and Van Haastert [24] have proposed a model for signal amplification with downstream cytosolic effector translocation. Their model describes a positive feedback mechanism involving phospholipid second messenger molecules. After application of an external gradient, the membrane receptors are activated and the production of phospholipid second-messenger molecules takes place at the front of the cell or at parts of the cell close to the external gradient source. The increase in the phospholipid second-messenger molecules makes the cytosolic effector molecules translocate from cytosol to the membrane at the front. Since there are more localized effector molecules near the front, the activated receptors on the outer membrane have more capability to induce the production of phospholipid second-messenger molecules. As an overall consequence, a positive feedback mechanism has

occurred in the phospholipid second-messenger molecules. The number of phospholipid second-messenger molecules will increase at the front and decrease at the back [24]. Gradient amplification in this case is defined to be the process of increasing differentiation between the front and the back of the cell.

Janetopoulos *et al.* [12] measured an amplification ratio of gradient sensing in *Dictyostelium* cells as the relationship between the levels of fluorescent intensity of Cy3-cAMP, a fluorescent cAMP analog that stimulates the cAMP receptors, and a fluorescently tagged readout protein (PH-GFP). The first one serves as chemoattractant or the input source and the latter is the measure of $PI(3,4,5)P_3$ recorded on the membrane. Their amplification ratio is defined as [12]:

$$\text{Janetoupoulos } \textit{et al.}\text{'s amplification ratio} = \frac{\text{normalized [PH-GFP]}}{\text{normalized [Cy3-cAMP]}} \tag{1.3.1}$$

The normalization in this sense means dividing each signal by its mean. The ratio is obtained from a least-squares fit. This measurement coincides agrees with Shibata and Fujimoto's characterization of signal amplification ratio [26], which is more generalized. They describe the amplification in terms of the gain g of the signal, defined by the ratio between the fractional change in the output signal X and the fractional change in the input signal Y.

$$g = \frac{\Delta X/\bar{X}}{\Delta Y/\bar{Y}}. \tag{1.3.2}$$

Janetopoulos *et al.* measured the amplification ratio based on the concentration of normalized PH-domain/GFP fluorescence signal *versus* normalized stimulus concentration. The resulting plot is shown in Figure 1, reproduced from [12]. In Section 2.7 we develop an alternative quantification of gradient signal amplification defined by the ratio of the dispersion of the output signal and the input signal.

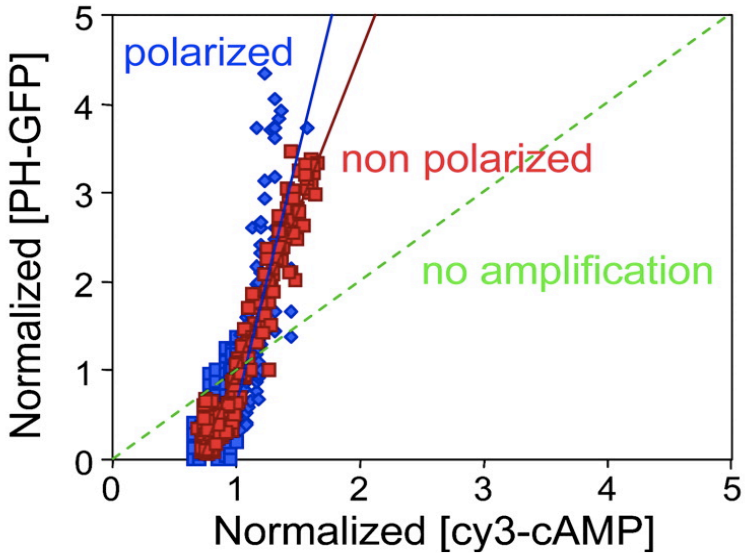

Figure 1: The amplification of the gradient signal interpreted as the ratio between the output (normalized [PH-GFP]) and input (normalized [cy3-cAMP]) signals. Normalization is multiplicative, so the plotted data have unit mean in along each direction. Reproduced from [12].

1.4 Models of Gradient Sensing Pathways

1.4.1 Deterministic Models

Alan Turing initiated the study of pattern formation in biological systems in terms of interactions of activation and inhibition mechanisms on different length scales [30]. Application of such reaction-diffusion systems of partial differential equations to pattern formation at the cellular level was spurred further by the work of Gierer and Meinhardt [7]. More recently, Levchenko and Iglesias derived a version of such a model based on a detailed molecular mechanism similar to that described in Section 1.3, namely activation of G-protein mediating both a locally acting activator (PI3K) and a globally acting inhibitor (PTEN) [17]. It is known as a local excitation, global inhibition (LEGI) principle. The scheme is implemented upon the assumption that a signal S triggers an activator A and an inhibitor B. The activator A catalyzes the conversion of a non-activated response factor R to an activated form R^*, whereas the

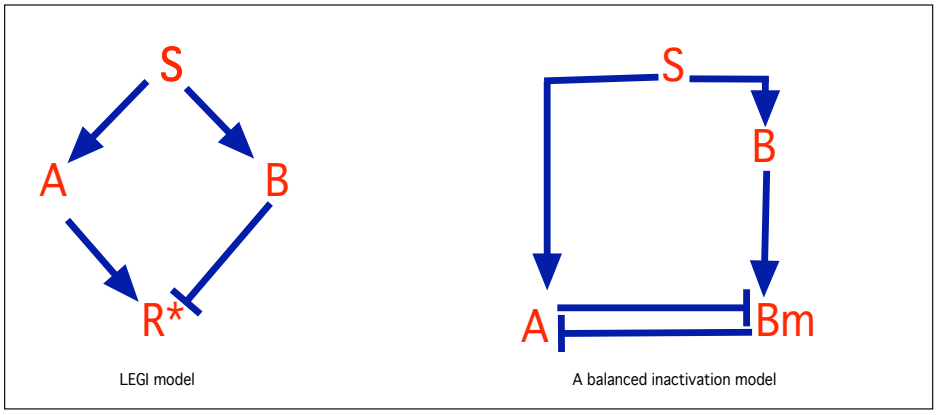

Figure 2: **[left]** A LEGI (local-excitation and global inhibition) model, which describes that the receptor occupancy signal (S) triggers a fast-local excitation signal (A) and a slow global inhibition signal B). Coupling both signals yield the cellular responses ($R*$). **[right]** A balanced inactivation model, which is a modification of LEGI incorporating a membrane-bound inhibitor (Bm) [10].

inhibitor I converts R^* into R [17]. Levchenko and Iglesias proposed chemical realization of this model; that S is the G-protein, A is PI3K, I is PTEN, R^* is PI(3,4,5)P_3 and R is phosphoinositide phosphate PI(4,5)P_2. The activation ceases when there is no PI3K. This characteristic of the LEGI model shows sensitivity to signal variation and changes in ligand concentration. However, the LEGI model does not account for a switch-like behavior observed in experiments that show the level of PH domain proteins approaches zero at the rear of the cell. This observation occurs for a wide range of chemoattractant gradients [12, 18]. Therefore, Levine *et al.* developed a balanced inactivation model, which is similar to the LEGI model, except it includes an additional component called a membrane-bound inhibitor acting as an inhibitor to the response [18]. Figure 2 shows the diagrams of LEGI and the balanced inactivation models. The difference is component Bm which acts as a membrane-bound inhibitor.

The balanced inactivation model describes the reactions of abstract components of gradient sensing mechanism [18]. The system of differential equation couples chemical

reactions happening on the cell membrane and the diffusion process of a cytosolic inhibitor, B. However, it excludes the external pathway of cAMP molecules binding to receptors. The system is described as below [18]:

$$\frac{\partial A}{\partial t} = k_a S - k_{-a} A - k_i A B_m, \tag{1.4.1}$$

$$\frac{\partial B_m}{\partial t} = k_b B - k_{-b} B_m - k_i A B_m, \tag{1.4.2}$$

$$\frac{\partial B}{\partial t} = D \nabla^2 B, \tag{1.4.3}$$

and dynamic boundary condition for diffusion equation,

$$D \overrightarrow{n} \cdot (\overrightarrow{\bigtriangledown} B) = k_a S - k_b B \tag{1.4.4}$$

where $\overrightarrow{n}$ represents the outward surface normal at each location on the boundary.

In this model, the component S represents the surface concentration of activated receptors, which is taken to be directly proportional to the concentration of chemoattractants. (This linearizing approximation mainly applies to weak gradients.) The activated receptors S generate membrane-bound species A and a cytosolic species B at rate k_a. The component A acts as an activator and also the cellular response to the gradient of the model. The molecule A degrades at rate k_{-a}. The component B acts as a cytosolic inhibitor. It is diffusible with diffusion coefficient equal to D. B can also binds to the membrane, producing a membrane-bound inhibitor B_m at rate k_b. B_m is also allowed to degrade at rate k_{-b}. The inhibiting reaction occurs by B_m reacting with A to form a complex $A \cdot B_m$ at rate equal to k_i. We interpret the vector sum of the locations of the remaining A molecules as representing the cell's inferred gradient direction. Equations (1.4.1) - (1.4.4) may be represented in terms

of chemical reactions as follows:

$$S \xrightarrow{k_a} A + B + S \tag{1.4.5}$$

$$A \xrightarrow{k_{-a}} \emptyset \tag{1.4.6}$$

$$B \xrightarrow{k_b} B_m \tag{1.4.7}$$

$$B_m \xrightarrow{k_{-b}} \emptyset \tag{1.4.8}$$

$$A + B_m \xrightarrow{k_i} A \cdot B_m \tag{1.4.9}$$

In equations (1.4.1) - (1.4.4), the quantities S, A and B_m are interpreted as the number of molecules per unit length (numbers per micron) along the membrane. The quantity B, in contrast, is represented as the number of molecules per unit area (number per square micron) in the interior of the cell. Consequently the constants k_a, k_{-a} and k_{-b} have units of 1/Time, while the constant k_i has units of Length/(Number·Time) and the constant k_b has units of Length/Time. The constants and parameters used are summarized in Table 1 and Table 2. In equation (1.4.4) the diffusion constant D has units of Length^2/Time and the gradient operator has units of 1/Length. Consequently the unit normal vector $\vec{n}$ is taken to be dimensionless.

Levine *et al.* showed that A localizes to the side of a model cell corresponding to a higher level of receptor occupancy S, while B_m localizes to the opposite side. They suggested that molecule A could be G_α which plays a role as activator and directs the pathway at the front, whereas $G_{\beta\gamma}$ could be thought as B molecules and control the localization at the back.

1.4.2 Stochastic Models

Berg and Purcell pointed out the importance of noisy fluctuations in local chemical concentrations, and fluctuations in receptor binding states, as providing a fundamental limit on the ability of cells to measure concentrations and gradients accurately [1]. They analyzed a model for chemotaxis in bacteria and calculated the statistical

noise that arises from variations in the number of receptors bound at any instant, caused by the random movement of ligand molecules near a single receptor molecule. They also noted that the accuracy in sensing chemical concentration depends on the number of receptors. Berg and Purcell's ideas were subsequently incorporated into stochastic models of chemotaxis in eukaryotic cells. Small bacterial cells (c. 1 μm in length) cannot accurately detect gradients by comparing receptor occupancies simultaneously at different points along their length, whereas larger amoeboid cells (c. 10 μm in diameter) can use a combination of spatial and temporal sensing. Tranquillo and Lauffenburger [28] developed a one dimensional model of the receptor population on the two sides of a lamellipodium (or leading edge). The key concept of Tranquillo's model is to evaluate the difference in the concentration associated with receptor binding, which is characterized as a Markov processes describing binding and unbinding of ligand with each membrane receptor. At the uniform chemoattractant concentration, the two sides of the lamellipod have about equal amounts of receptors bound to ligand. Therefore, the direction that the cell moves is at the middle between two sides. If the gradient source is placed near the right side, the number of receptors perceiving ligand concentration is more than the left and hence cell turns toward the right. The fluctuation in the direction is mainly from the error in the binding ability of receptors. In order to account for the effects of fluctuations internal to gradient sensing pathways, we need to account for the random occurrence of events generated from chemical reactions and the transmission of noise throughout the pathway.

Shibata and Ueda used a simple scheme to elucidate noise propagation and its effect to the accuracy of chemotaxis in *Dictyostelium* [27]. As discussed in Section 1.3, the gain represents the cellular response. For the pathway that involves multiple reactions, the noise propagates through the system. Shibata and Ueda consider the noise transmitted by other reactions and the noise generated by input signals to be extrinsic noise, whereas intrinsic noise is the noise of output signal that can be calculated by the difference between output signal and the output signal at steady

state. Shibata and Ueda calculated a signal to noise ratio (SNR) for different ligand concentration conditions. They found that at the lower ligand concentration, SNR is mainly affected by extrinsic noise. This implies ligand binding fluctuation determines the accuracy of gradient sensing. For a higher ligand concentration, the intrinsic noise contributes dominantly [27]. For the purposes of this thesis we have focused on implementing representations of noise internal to the signaling pathway, although it should be straightforward to include noise due to receptor occupancy fluctuations as well.

2 Methods

2.1 Deterministic point model

When the diffusion coefficient D is large , the number of molecules B inside the cell is uniformly distributed. As a consistency check, we compare the steady state response to a uniformly applied signal with simulations of the 2D model for large values of D.

To find the steady state to a uniform signal given a concentration of chemoattractants equal to S_0, we set the right hand sides of equations (1.4.1)-(1.4.4) equal to zero and solve to obtain B, B_m and A at steady state [18].

Setting (1.4.4) equal to zero yields B at steady state, B_0.

$$B_0 = \frac{k_a S_0}{k_b}. \tag{2.1.1}$$

Then, solving (1.4.1) and (1.4.2) with $B = B_0$ gives A_0 and $B_{m,0}$.

$$B_{m,0} = \frac{k_b B_0}{k_i A_0 + k_{-b}} \tag{2.1.2}$$

$$A_0 = \frac{-k_{-a}k_{-b} + \sqrt{(k_{-a}k_{-b})^2 + 4k_a k_i k_{-a} k_{-b} S_0}}{2k_i k_{-a}} \tag{2.1.3}$$

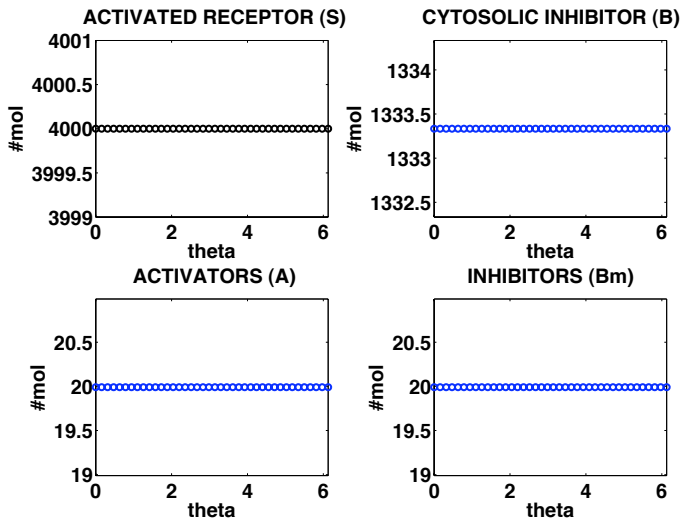

Figure 3: The result of deterministic point model analytically solved with $S_0 = 4000$ molecules per node and the constant parameters as specified in Table 1 and Table 2. **Top Left:** the number of chemoattractant molecules S at t = 0s. **Top Right:** the number of cytosolic B per node (at the membrane) at steady state. **Bottom:** the number of membrane bound A (**Left**) and B_m (**Right**) at steady state.

Figure 3 illustrates the result when uniformly distributed chemoattractant is applied. Figure 3A shows the concentration of input (activated receptor molecules) uniformly distributed around the cell membrane, 4000 molecules per node ($\#mol/node$). The 40 nodes on the cell membrane are distributed evenly, with a spacing of $(10\pi/40)\mu$m $\approx$ 0.785μm, as in the cell geometry depicted in Figure 5. At steady state, the cytosolic molecules B present at the membrane nodes is also uniformly distributed as shown in Figure 3B. Consequently, the induced products A and B_m are uniformly distributed on the cell membrane. Section 3 shows the result of stochastic simulation with the same parameters assigned. The stochastic simulation converges to a distribution close to that predicted by the deterministic point model.

2.2 Multinomial Representation of Chemical Reactions

2.2.1 Chemical reactions and spatial transitions represented *via* discrete time, discrete space stochastic processes

The LEGI and Balanced Inactivation Models were originally formulated as partial different equations models in which a reaction-diffusion system in the cell interior is coupled to a system of nonlinear differential equations localized to each point of the boundary. The model variables located on the cell membrane boundary are also coupled to the external reaction-diffusion system representing the external signal. We call this type of system a *boundary-coupled reaction diffusion PDE system*, because the interior and exterior of the model cell are coupled only through the boundary variables. The standard modeling approach through boundary coupled PDEs does lend itself to studying the variability in cellular response. A model cell with uniform initial conditions placed in a linear gradient will, by virtue of reflectional symmetry, always have an extremum of the internal signaling components along the axis parallel to the gradient direction. However, real cells performing chemotaxis show a distribution of movement directions relative to the stimulus direction [28]. Fluctuations in the signaling pathways due to molecular counting noise have been proposed as an important source of behavioral and phenotypic variability in chemotaxis [25, 29], as well as genetic regulatory and other systems [5].

As Shibata has pointed out [27] the same processes that amplify an extracellular gradient signal will also amplify the fluctuating component (noise) inherent in the pathway upstream of the amplification process. Moreover the reactions responsible for amplification may contribute additional noise. In order to account for the discrete and stochastic nature of the gradient sensing system, we adopt a chemical master equation (CME) approach.

Gradient sensing mechanism is susceptible to noise amplification [26, 27]. Therefore, we should account for the discrete and stochastic nature of the system. The

chemical master equation (CME) is used to capture the variation in chemical species as a parabolic partial differential equation with the prerequisite that the system can be regarded as a Markov process and its content is well-mixed. However, the size of the state space grows exponentially with the number of reactant species in the model. Direct ("exact") solution methods can be cumbersome even with few chemical species involved. The most common strategy for handling a large state space is the stochastic simulation algorithm (SSA) [8]. The SSA simulates the chemical evolution by randomly applying the reactions of the system and recording the resulting states. The simulated data is then used to estimate a probability density function. To accelerate simulation speed, Gillespie proposed a scheme called a τ-leaping method [8], where the exponential waiting time, τ, for the next reaction to occur is improved. The reactions likely to occur are drawn from a longer time step, τ, from either a Poisson or Binomial distribution. However, for a balanced inactivation model, the well-mixedness assumption does not apply since the probability of reacting molecules also depends on their locations on cell's boundary. The multinomial simulation algorithm (MSA) was introduced to account for spatial inhomogeneity [16]. The system is divided into subvolumes each of which is assumed to be well mixed. We use the idea of MSA to apply to the balanced inactivation model.

The probability distribution governing the occurrence of reactions in a chemical master equation formulation depends on the type of each reaction. Therefore we categorized the chemical reactions (1.4.5)-(1.4.9) into zeroth order, first order, and second order reactions.

The only zeroth order reaction is the reaction (1.4.5). In a time interval dt, N_S molecules of S independently induce reaction (1.4.5) with intensity $N_S k_a dt$. It is similar to a birth process which obeys a Poisson distribution. We assume that the S molecules, which also represent the chemoattractant molecules, are distributed

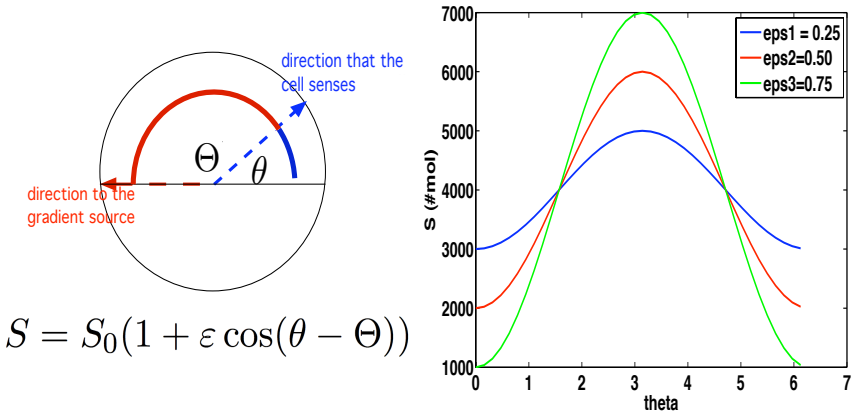

Figure 4: **[left]** The concentration of activated receptors in linear gradient with various gradient constant, ε, $S_0 = 4000$ molecules, and $\Theta = \pi$

following a linear gradient according to the formula:

$$S(\theta) = S_0(1 + \varepsilon \cos(\theta - \Theta)), \tag{2.2.1}$$

where θ is a directional variable of the cell in circular shape, $0 \leq \theta \leq 2\pi$, Θ is a parameter of the true direction where the gradient source is placed, S_0 is the median concentrations of S molecules around the cell membrane and $0 \leq \varepsilon \leq 1$ is the relative or fractional gradient parameter. In Figure 4, the relative gradient constant (ε) shapes the steepness of gradient in chemoattractants. Therefore, we can draw a random number for the reaction (1.4.5) to occur following the Poisson distribution:

$$\Delta N_A(dt)_{S \to A+B+S} = \Delta N_B(dt)_{S \to A+B+S} \sim \text{Poiss}(N_S k_a dt) \tag{2.2.2}$$

Because the source S is taken to be constant in time, this expression is valid for arbitrarily long time intervals dt.

The first order reactions are the reactions (1.4.6), (1.4.7) and (1.4.8). Each molecule on the membrane has two choices; to react or stay calm. Each molecule A, B and B_m has a chance to participate in the reactions with probabilities equal

to $k_{-a}dt$, $k_b dt$ and $k_{-b}dt$ respectively. In order words, provided the numbers of each molecule remains fixed in a given (short) time interval dt, the number of instances of each reaction occurring within dt obeys the binomial distribution:

$$\Delta N_A(dt)_{A\to\phi} \sim \text{Binom}(N_A, k_{-a}dt) \tag{2.2.3}$$

$$\Delta N_B(dt)_{B\to B_m} \sim \text{Binom}(N_B, k_b dt) \tag{2.2.4}$$

$$\Delta N_{Bm}(dt)_{B\to\phi} \sim \text{Binom}(N_{Bm}, k_{-b}dt). \tag{2.2.5}$$

For the bimolecular reaction (1.4.9), the probability of the reaction occurring n times in an interval dt cannot be drawn directly from a Binomial or Poisson distribution due to the depletion of both reactants A and Bm. Let $p_n(t)$ be the probability that as of time t exactly n reactions have occurred. Suppose N_{A0} and N_{Bm0} are the initial numbers of molecules A and Bm. Then the probability that *no* bimolecular reactions have occurred in time t decays exponentially at rate $N_{A0}N_{Bm0}k_i$:

$$p_0(t) = \exp(-N_{A0}N_{Bm0}k_i t). \tag{2.2.6}$$

For the probability of exactly $0 < n \leq \min(N_{A0}, N_{Bm0})$ reactions to have occurred in time t, we have the recurrence relation

$$\frac{dp_n(t)}{dt} = \left(-Q(n)p_n(t) + Q(n-1)p_{n-1}(t)\right) k_i, \tag{2.2.7}$$

where we define the quadratic factor $Q(n)$ as

$$Q(n) = (N_{A0} - n)(N_{Bm0} - n). \tag{2.2.8}$$

However, with higher n, we encounter difficulty in solving for the general case of differential equation (2.2.7). Instead we invoke Kurtz's theorem, which guarantees the convergence of the mean of the master equation solution to the deterministic system

in the limit of large numbers of (well mixed) reacting molecules. The deterministic rate for the bimolecular reaction is

$$\frac{dN_A}{dt} = \frac{dN_{B_m}}{dt} = -\frac{dN_{A\cdot B_m}}{dt} = k_i N_A(t) N_{B_m}(t) = -k_i Q(N_{A\cdot B_m}). \tag{2.2.9}$$

where we temporarily abuse notation, *e.g.* using N_A to refer to the expected value of N_A, for sufficiently large N_A and N_{B_m}. For this equation we assume an initial value of $N_{A\cdot B_m}(0) \equiv 0$.

Converting equation (2.2.9) to a logistic growth equation gives

$$\frac{du}{dt} = ru(1 - \frac{u}{K}), \tag{2.2.10}$$

where

$$u(t) = \max(N_{A0}, N_{B_m 0}) - N_{A\cdot B_m}(t); \tag{2.2.11}$$

$$r = k_i |N_{A0} - N_{B_m 0}|; \tag{2.2.12}$$

$$K = |N_{A0} - N_{B_m 0}|. \tag{2.2.13}$$

Solving equation (2.2.10) yields an expression for the change in $N_{A\cdot B_m}$, which corresponds to the mean number of reactions,

$$N_{A\cdot B_m} = N_{A0} - N_A(t) = N_{B_m 0} - N_B(t). \tag{2.2.14}$$

$$N_{A\cdot B_m} = \begin{cases} N_{B_m 0}\left(1 - \frac{N_{B_m 0} - N_{A0}}{N_{B_m 0} - N_{A0}\exp(-(N_{B_m 0} - N_{A0})k_i t)}\right), & N_{B_m 0} > N_{A0} \\ N_{A0}\left(1 - \frac{N_{A0} - N_{B_m 0}}{N_{A0} - N_{B_m 0}\exp(-(N_{A0} - N_{B_m 0})k_i t)}\right), & N_{A0} > N_{B_m 0} \\ N_{A0}\left(1 - \frac{1}{1 + N_{A0} k_i t}\right), & N_{A0} = N_{B_m 0}. \end{cases} \tag{2.2.15}$$

This expression gives an approximation for the number of times the bimolecular reaction (1.4.9) occurs in a time interval of length t, given the initial number of molecules of A and B_m. Therefore, we draw the number of molecules A and B_m that will be depleted due to reaction (1.4.9) from a binomial distribution represent-

ing $n_{\max} = \min(N_{A0}, N_{Bm0})$ independent samples each with probability given by $N_{A \cdot B_m}/n_{\max}$, where $N_{A \cdot B_m}$ is calculated from 2.2.15 with time interval dt.

$$\Delta N_A(dt)_{A+B_m \to A \cdot B_m} = \tag{2.2.16}$$
$$N_{B_m}(dt)_{A+B_m \to A \cdot B_m} \sim \text{Binom}\left(\min(N_{A0}, N_{B_m 0}), \frac{N_{A \cdot B_m}}{\min(N_{A0}, N_{B_m 0})}\right)$$

At this point, we know how to estimate the increments and decrements of molecules A, B and B_m that participate in reactions (1.4.5) - (1.4.9) for each time step on the membrane, for each reaction type (zeroth order, first order, second order) taken singly. In practice, we interleave each reaction type rather than execute each simultaneously (see Section 2.4 for details of the simulation algorithm). It remains to address the spatial distribution of the cytosolic diffusible molecule B. The next section will introduce how to solve for the number of molecules B at each internal node. Coupling both membrane reactions and diffusion process will make the simulation in 2D of reactions (1.4.5) - (1.4.9) complete.

2.2.2 Representation of Diffusion *via* Finite Elements

Using a finite element method provides geometrical flexibility and allows us to manipulate the internal nodes directly. In order to implement the balanced inactivation model with a finite element method, we need to generate a triangular mesh for the two dimensional disk-shaped cell. Using COMSOL, we generated an irregular triangular mesh comprising 216 vertices, 40 of which are on the circular domain boundary, and 390 triangles (see Figure 5). Following triangulation, the model was implemented using two 40-component vectors to represent the number of molecules of A and B_m at each node of the boundary, respectively, and a vector of 216 components to represent the number of cytosolic (not membrane bound) molecules of B at each node. The finite element method allows us to present the diffusion of B with a flux boundary condition, according to equations (1.4.3)-(1.4.4), using the Galerkin finite element

method (GFEM) [15].

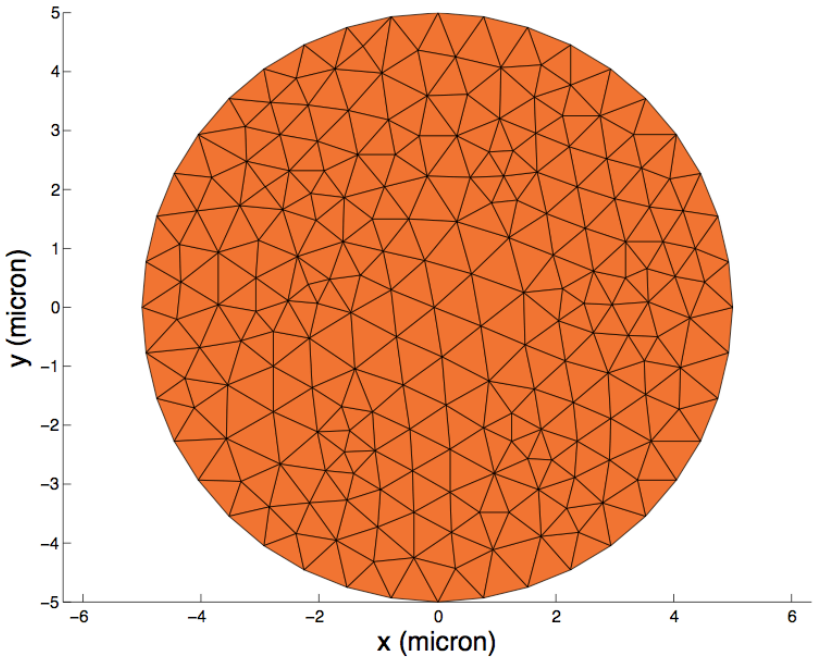

Figure 5: Two dimensional simulation geometry. The simulated cell is taken to be a disk of radius five microns centered at coordinates $(0, 0)$. The triangulation of the cell shape, generated by the COMSOL finite element package, contains 40 boundary nodes and 390 triangles.

For this diffusion problem, the diffusion equation in terms of the Cartesian coordinate system is

$$D\left(\frac{\partial^2 B}{\partial x^2}+\frac{\partial^2 B}{\partial y^2}\right)=\frac{\partial B}{\partial t}. \tag{2.2.17}$$

The boundary condition is dynamic since the variables S and B may change in time:

$$D\overrightarrow{n}\cdot(\overrightarrow{\nabla}B)=k_aS-k_bB \tag{2.2.18}$$

where $\overrightarrow{n}$ is the dimensionless outward normal unit vector, see Section 1.4.1.

The goal of GFEM is to find an approximate solution, $\tilde{B}$, such that the integration of the weighted residual, I, over the domain, Ω, vanishes.

$$I=\int_\Omega\left[wD\left(\frac{\partial^2 B}{\partial x^2}+\frac{\partial^2 B}{\partial y^2}\right)-\frac{\partial B}{\partial t}\right]d\Omega-\int_\Gamma wD\vec{n}\cdot\vec{\nabla}B\,d\Gamma, \tag{2.2.19}$$

where Γ is the boundary of the domain Ω and w is the Galerkin's weighted function.

More specifically, we approximate B *via* linear interpolation within each element:

$$B \approx \tilde{B} = a_1 + a_2 x + a_3 y, \tag{2.2.20}$$

or

$$\tilde{B} \approx \begin{pmatrix} 1 & x & y \end{pmatrix} \begin{pmatrix} a_1 \\ a_2 \\ a_3 \end{pmatrix}. \tag{2.2.21}$$

Therefore, the linear interpolation for each triangular element (see Figure 5) is represented by

$$\begin{pmatrix} \tilde{B}_1 \\ \tilde{B}_2 \\ \tilde{B}_3 \end{pmatrix} = \begin{pmatrix} 1 & x_1 & y_1 \\ 1 & x_2 & y_2 \\ 1 & x_3 & y_3 \end{pmatrix} \begin{pmatrix} a_1 \\ a_2 \\ a_3 \end{pmatrix}. \tag{2.2.22}$$

Solving for the unknown coefficients a_i gives

$$\begin{pmatrix} a_1 \\ a_2 \\ a_3 \end{pmatrix} = \frac{1}{2\Lambda} \begin{pmatrix} x_2 y_3 - x_3 y_2 & x_3 y_1 - x_1 y_3 & x_1 y_2 - x_2 y_1 \\ y_2 - y_3 & y_3 - y_1 & y_1 - y_2 \\ x_3 - x_2 & x_1 - x_3 & x_2 - x_1 \end{pmatrix} \begin{pmatrix} \tilde{B}_1 \\ \tilde{B}_2 \\ \tilde{B}_3 \end{pmatrix} \tag{2.2.23}$$

where

$$\Lambda = \frac{1}{2} \det \begin{pmatrix} 1 & x_1 & y_1 \\ 1 & x_2 & y_2 \\ 1 & x_3 & y_3 \end{pmatrix}. \tag{2.2.24}$$

Substituting (2.2.7) into (2.2.5) yields

$$\tilde{B} = \tilde{w_1}(x, y)\tilde{B}_1 + \tilde{w_2}(x, y)\tilde{B}_2 + \tilde{w_3}(x, y)\tilde{B}_3 \tag{2.2.25}$$

where

$$\tilde{w} = \begin{pmatrix} \tilde{w_1}(x,y) \\ \tilde{w_2}(x,y) \\ \tilde{w_3}(x,y) \end{pmatrix} = \begin{pmatrix} \frac{1}{2\Lambda}[(x_2y_3 - x_3y_2) + (y_2 - y_3)x + (x_3 - x_2)y] \\ \frac{1}{2\Lambda}[(x_3y_1 - x_1y_3) + (y_3 - y_1)x + (x_1 - x_3)y] \\ \frac{1}{2\Lambda}[(x_1y_2 - x_2y_1) + (y_1 - y_2)x + (x_2 - x_1)y] \end{pmatrix}. \tag{2.2.26}$$

Therefore, the weighted function for Galerkin's method, $w_i = \frac{\partial \tilde{B}}{\partial a_i}$, is

$$w = \tilde{w}. \tag{2.2.27}$$

Substituting w into equation (2.2.19) and solving for B, we should obtain an approximate solution of the diffusion problem.

2.3 Markov representation of chemical reactions and spatial transitions

2.3.1 Diffusion represented as a Markov process on a graph

In order to further the long range goal of realizing a fully stochastic representation of an intracellular signaling pathway, we set out to implement a stochastic model of diffusion compatible with a finite element representation. Viewing the 216 vertices of the triangulation as the nodes of a graph, we can think of molecules of B "diffusing" by performing a random walk from node to node along the edges of the triangles. If we let the vector $p(t) \in \mathbb{R}^{216}$ represent the probability of finding a random walker at each node (so we require $0 \leq p_i(t)$ and $\sum_{i=1}^{216} p_i(t) \equiv 1$ for all t) then the evolution of diffusion represented as a Markov process on the graph obeys a linear equation

$$dp/dt = Qp. \tag{2.3.1}$$

The Markov transition matrix Q satisfies $Q_{ij} > 0, i \neq j$, and $\sum_i Q_{ij} = 0$. Given N random walkers moving independently with identical probability distributions p

on the graph, the expected number of walkers present at node i at time t is just $\bar{n}(t) = Np_i(t)$. Hence the expected number $\bar{n}(t)$ obeys the same linear differential equation

$$d\bar{n}/dt = Q\bar{n}.$$

Can we obtain an appropriate matrix Q by considering the corresponding finite element solution to the diffusion problem? The finite element representation of pure diffusion with zero flux boundary conditions leads to a linear differential equation of the form

$$M\dot{u} = Ku$$

where $u \in \mathbb{R}^{216}$ represents the (time varying) concentration at each node. If we define the j^{th} shape function $\phi_j(x, y)$ to be piecewise linear on each triangle with $\phi_i(x_j, y_j) \equiv \delta_{ij}$ then we can define the mass and stiffness matrices respectively as

$$\begin{aligned} M_{ij} &= \int_\Omega \phi_i \phi_j \, dx \, dy \\ K_{ij} &= \int_\Omega \nabla(\phi_i) \cdot \nabla(\phi_j) \, dx \, dy. \end{aligned}$$

In the finite element formulation the entries of u represent the linearly interpolated *concentration* of a quantity at each point. To convert between concentrations and numbers requires knowing the volume associated with each node. In the linear interpolating finite element case this is straightforward. The piecewise linear shape functions form a partition of unity, $\sum_i \phi_i(x, y) \equiv 1$ for all $(x, y) \in \Omega$. Hence the total two dimensional "volume" (i.e. the area) of the domain Ω is

$$V \equiv \int_\Omega 1 \, dx \, dy = \sum_{i=1}^{216} \int_\Omega \phi_i(x, y) \, dx \, dy.$$

It is natural to denote the integrals $\int_\Omega \phi_i(x, y)$ as the area associated with each node. It is straightforward to show that this quantity is equal to one third the sum of the

areas of the triangles that include node i as one vertex.

Define the 216×216 diagonal matrix V such that v_{ii} is the area v_i associated with the i^{th} element. Then the expected number of random walkers at each node is related to the concentration as $u_i = \bar{n}_i / v_i$, or

$$u(t) = V^{-1}\bar{n}(t).$$

Differentiating in time, we find that

$$d\bar{n}/dt = VM^{-1}KV^{-1}\bar{n},$$

which suggests setting $Q_0 = VM^{-1}KV^{-1}$ should be a reasonable choice for a Markov transition matrix. However, several difficulties arise.

1. While M_{ij} and K_{ij} are sparse (713 out of 23220 (i, j) pairs of entries are nonzero), the matrix Q_0 is not sparse – in fact it contains no zero entries. Hence "diffusion" occurs not just between adjacent nodes but between nodes arbitrarily far apart, which does not comport well with physical intuition about diffusion as a continuous process.

2. For a standard linear finite element scheme as shown in Figure 5, roughly half the entries of Q_0 are positive and half are negative. To be interpreted as transition rates the off diagonal entries of a Markov transition matrix should all be nonnegative. The mean of Q_0 is within machine precision of zero. The entries of Q_0 are distributed around this mean with a standard deviation (including diagonal terms) of about 600. While most of the negative entries are clustered near zero, over a thousand are negative by more than one standard deviation.

3. Each column of Q should sum to zero, but due to accumulating numerical error the columns of Q_0 sum to positive or negative quantities on the order of 10^{-10}, leading to local violation of conservation of mass.

In order to circumnavigate this problem we explored alternative means of representing the diffusion process using a Markov transition matrix. In the end, the results were not satisfactory, and we only included deterministic representations of diffusion (both the finite-element and Markov transition matrix based) in the simulations.

2.3.2 Calculation of a transition matrix for a diffusion process

We exploit the structure of finite-element numerical models to illustrate our approach to generate a Markov transition matrix for diffusion problems. In a model of diffusion without drift and without source or sink terms, the steady state should correspond to the uniform concentration over the entire domain. The Markov chain on the graph refers to the probability of a particle residing at each of the nodes. Note that in the case of generic finite elements, nodes are nonuniform in shape and size. Consequently uniform spatial distribution of concentration and uniform nodal distribution of probability are different.

Suppose the coefficients of an approximate linear interpolant solution are $c_i(t)$ with the linear approximate solution $\tilde{c}(x,t)$ given by

$$\tilde{c}(x,t) = \sum_i c_i(t)\phi_i(x), \tag{2.3.2}$$

and at the uniform concentration steady state $c_i(t) = m_i/v_i$ where m_i is the number of particles at node i and v_i is volume associated with node i. The V stands for the volume[1] of the domain. As discussed above, the volume associated with any given node is

$$v_i = \int_x \phi_i(x)\, dx \tag{2.3.3}$$

and the probability of a random walker residing "at" node i is $v_i c_i(t)$.

As an example, consider a linear domain $x \in [0,1)$ with periodic boundary condi-

[1] In 1D "volume" refers to length; in 2D it refers to area; *etc.*

tions and nodes at

$$20x_i \in \{0 \equiv 20, 1, 2, 3, 4, 5, 7,\ 9,\ 11,\ 13,\ 15, 16, 17, 18, 19\}$$

with linear interpolant finite elements. The element volumes are

$$v_i = \begin{cases} 2/40, & i = 16, 17, 18, 19, (20 \equiv 0), 1, 2, 3, 4 \quad (9 \text{ nodes}) \\ 3/40, & i = 5, 15 \quad (2 \text{ nodes}) \\ 4/40, & i = 7, 9, 11, 13 \quad (4 \text{ nodes}) \end{cases}$$

which sums to unity. These also must be the probabilities of finding a random walker at any given node once the system has reached its equilibrium distribution.

In general, at steady state the probability of an arbitrary particle being at node i out of N nodes total should not be $1/N$ but rather

$$p_i(\infty) = \frac{c_i(\infty)v_i}{M} = \frac{v_i}{V} \tag{2.3.4}$$

i.e. the fraction of the total volume associated with node i. The requirement of detailed balance at equilibrium dictates that for each pair of nodes (i, j) the following condition holds:

$$q_{ji}p_i(\infty) = q_{ij}p_j(\infty) \tag{2.3.5}$$

where q_{ji} is the rate of flow per particle from node i into node j (see Figure 6). Combining the equations (2.3.4) and (2.3.5) gives

$$q_{ji}v_i = q_{ij}v_j. \tag{2.3.6}$$

One way to choose a transition matrix, Q, whose entries q_{ij} are consistent with a

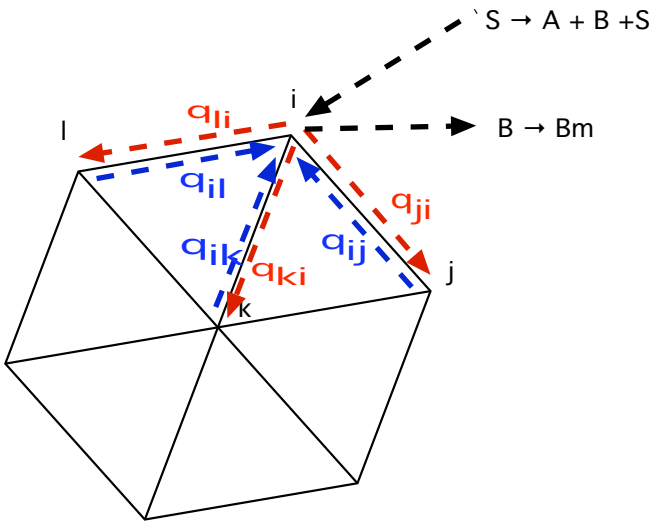

Figure 6: Illustration of the transitions representing diffusion. A molecule of cytosolic B located at boundary node (i) can make a transition to a neighboring internal node (k), to one of the neighboring boundary nodes $(j, l)^2$ In addition molecules of B are introduced to the cytosol at the boundary nodes by the source S, and are removed from the cytosol through the inhibitory reaction $B \rightarrow B_m$ occurring at the boundary nodes.

uniform concentration at steady state, is to set

$$q_{ji} = \sqrt{\frac{v_j}{v_i}}, (i \neq j) \tag{2.3.7}$$

$$q_{ii} = -\sum_j q_{ji} \tag{2.3.8}$$

(In practice, we rescale Q so that it has norm 1 before proceeding further. As described below, an additional rescaling of Q will allow us to accommodate an arbitrary value for the physical diffusion constant.) Therefore the matrix Q containing entries q_{ij} for i and j = 1,2,3,...,N serves as a Markov transition matrix. The first order transitions above are equivalent to having a continuous time Markov process on the network of nodes. Such a system obeys

$$dp/dt = Qp$$

where p is a probability vector and Q is a Markov transition rate matrix.

However, the matrix Q is a fixed valued matrix. Assume that $\text{norm}[Q] = 1$. For the purpose of adjusting Q to agree with the diffusion constant, we need to scale Q so that the growth rate of the variance of particle's position is a constant, $d\mathbb{V}[X_t]/dt = \lambda$. The explanation of why scaling Q makes the markov transition agree with the diffusion constant is discussed in Section 2.8.

Figure 7 shows the result of using a matrix Q without this corrective scaling to represent a diffusion process. Assume that at time $t = 0$ s, 2000 molecules of B are placed at the center of the domain, i.e. the origin in our geometry. After allowing the dispersion to go for 0.2 s with diffusion constant $D = 10\ \mu m^2/s$, the growth of the variance in the model representing the expected Markov transition rates (red line) is much different to the growth of the variance in finite element model (blue line) where the given diffusion constant has been accounted for automatically by the COMSOL software. Therefore we scale matrix Q by the ratio between the growth rate of the variance in the finite element model and the growth rate of the variance in Markov model. Figure 8 shows the result after we scaled Q. Both plots of variance of particle's position match well. We will use this scaled Q for the Markov transition matrix in diffusion process with a specified diffusion constant.

2.3.3 Markov approximation of diffusion *via* a linear interpolating finite element construction

This section describe how we use the Markov transition matrix calculated by the previous section to solve for the expected number of particles at each time step. At each time step, the change in number of molecule A and the number of molecules B_m located on the membrane have been described in equation (1.4.1) and (1.4.2). More specifically, at node i at time t, the change in number of molecule A and molecule

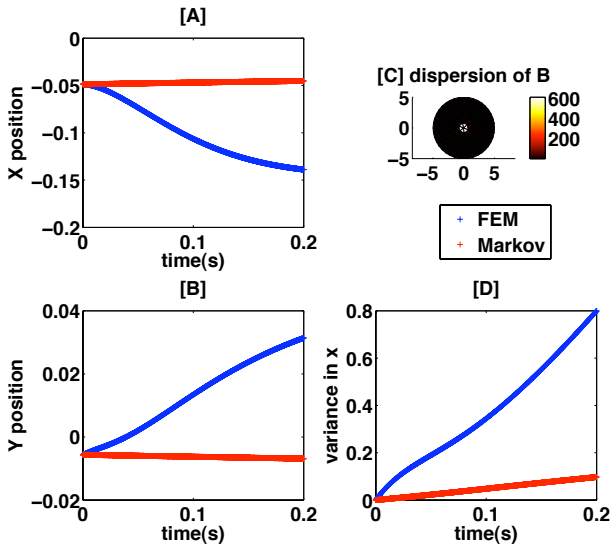

Figure 7: **[left]** Plots [A] and [B] represent the evolution of mean position in x and y components respectively of a random walker begun near (0,0). **[right]** Plot [C] shows how B molecules originally placed at the origin disperse when t = 0.2 s. Plot [D] is the evolution of variance in x-position of both finite element model (blue line) and the Markov transition model (red line). The discrepancy is addressed by rescaling the Markov transition matrix Q.

B_m are as described in Figure 6.

$$dA_i(t)/dt = (k_a S_i - k_{-a} A_i - k_i A_i B m_i) \tag{2.3.9}$$

$$dBm_i(t)/dt = (k_b B_i - k_{-b} B m_i - k_i A_i B m_i). \tag{2.3.10}$$

Note that B_i in the equation (2.3.10) refers to molecule B located on the cell membrane. Membrane bound molecules of B occur only on the boundary nodes in the cell geometry (Figure 5). However the change in molecule B as described in equation (1.4.3) involves the transition among both interior and exterior nodes. That makes B transits to the neighbor nodes as it diffuses.

$$dB_i(t)/dt = \sum_j q_{ij} B_j - \sum_j q_{ji} B_i + (k_a S_i - k_b B_i) \tag{2.3.11}$$

Solving for variable A, B and B_m for each time step complete the model simulated

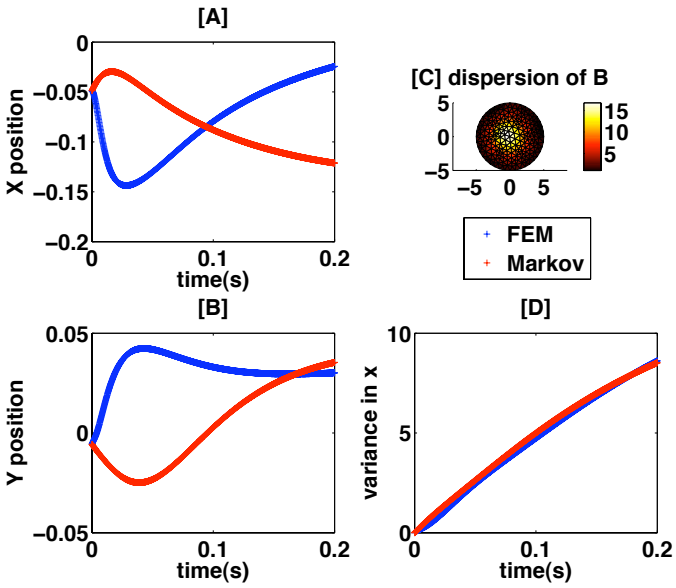

Figure 8: **[left]** Plots [A] and [B] represent the evolution of mean position in x and y components respectively of a random walker began near (0,0). **[right]** Plot [C] shows how 2000 molecules of B originally placed at the origin disperse when t = 0.2 s. Plot [D] is the evolution of variance in x-position of both finite element model (blue line) and the Markov transition model (red line), using the rescaled transition matrix.

via Markov transition matrix or the expected model.

2.4 Simulation Algorithm

Integrating the methods for both stochastic and markov-transition processes, we simulate a balanced inactivation model following the algorithm:

1. Initialize parameters and a geometry domain. The geometry domain is a two-dimensional disk with radius = 5 μm. We triangulated into 390 triangles for the purpose of calculation using finite elment method and Markov transition matrix. The geometry in Figure 5 shows that we have 216 nodes in total with 40 nodes located on cell boundary. The parameters used in this model are specified in Table and 1 and Table 2. Then, follow the method Section 2.3.2. to find the scaled transition matrix Q.

2. Solve for initial conditions based on steady state solution for homogeneous problem. This implementation of this step follows the formula (2.1.1) - (2.1.3).

3. Main iteration

   The main iteration is a loop going one time step until the final time has reached. In the main iteration, two simulated models. One used the stochastic transitions (except for diffusion of cytosolic B, which used the Markov transition matrix but was represented as a deterministic process); and one which used the expected value for the change due to each reaction at each time step. We call the two models the "stochastic" and the "expected value" models, respectively. For each model we recorded the values of A, B and B_m for every node at each time step.

   Initialize vectors $\overrightarrow{sA}$, $\overrightarrow{sB}$ and $\overrightarrow{sBm}$ to store the numbers of molecules A, B and B_m respectively at every node for the simulation of stochastic model. Also initialize vectors $\overrightarrow{nA}$, $\overrightarrow{nB}$ and $\overrightarrow{nBm}$ to store the numbers of molecules A, B and B_m respectively at every node for the expected Markov transition-matrix model.

   for time t = 0 to t = 0.2 sec.

   Stochastic Model

   (a) Update second order reactions. Generate a random number based on binomial distribution with parameters specified in the formula (2.2.15) to approximate change in number of A and Bm. Decrement both sA and sB_m by that number.

   (b) Update first order reactions. Generate three random numbers based on binomial distribution following the formulas (2.2.3), (2.2.4) and (2.2.5) respectively. Decrement sA by the random number for the degrading of A reaction . Decrement sB and at the same time increment sB_m by the

random number for the conversion of B to B_m reaction. Lastly, decrement sB_m by the random number for degrading of B_m

(c) Update zeroth order reactions. Generate a random number based on Poisson distribution. Increment the number of sA and sB that locate on boundary.

(d) Update the number of molecule sB at every nodes in the domain *via* the finite element method solving the diffusion problem described in Section 2.2.2.

Expected markov-transition model

(a) Update nA following the equation (2.3.9), $nA(t+1) = nA(t) + dA(t)$.

(b) Update nBm following the equation (2.3.10), $nBm(t+1) = nBm(t) + dBm(t)$.

(c) Update nB following the equation (2.3.11), $nB(t+1) = nB(t) + dB(t)$.

4. visualization / output

2.5 Estimating Direction in the Balanced Inactivation Model

The "readout" of the direction physically corresponds to a biochemical/mechanical process in which the cell generates a pseudopod and advances in a certain direction. Instead of modeling this process we interpret the output of the simulation (the random distributions of $\{A_i, Bm_i\}$) as specifying the direction the cell would next extend a pseudopod. In Levine *et al.* [18] the direction of movement is interpreted as the localization of A around perimeter of the cell. We choose to implement a vector sum model for the cell's decision process (mean direction in the sense of circular random variables [20].)

If θ is the directional variable with n observation, the vector mean direction ($\bar{\theta}$) as circular mean can be calculated from:

$$\hat{S} = \sum_{i=1}^{n} \frac{m_i}{M} \sin\theta_i,$$
$$\hat{C} = \sum_{i=1}^{n} \frac{m_i}{M} \cos\theta_i,$$

$$\bar{\theta} = \arctan(\hat{S}/\hat{C}). \tag{2.5.1}$$

The mean resultant length is

$$\bar{R} = \sqrt{\hat{S}^2 + \hat{C}^2}/n. \tag{2.5.2}$$

The input vector in this case is the vector $\overrightarrow{A}$ containing the number of molecules A at each boundary node so that $n = 40$.

2.6 Circular Variance

Given a way of choosing a direction based on different stages of the cell's signaling pathway, we obtain an ensemble of different direction choices for any given set of stimulus parameters (mean concentration $\bar{c}$ and relative gradient $|\nabla c|/\bar{c}$). By symmetry the mean direction of the ensemble is always correct, but what is of interest is the variability of the directional estimate from trial to trial or from cell to cell. We quantify the accuracy of the cell's directional estimate by finding the circular variance of the distribution of estimates over many trials.

With various directions of gradient sources, the concentrations of cytosolic inhibitor B, activator A and inhibitor B_m tend to follow the *von Mises distribution*, which is known as the circular normal distribution. The von Mises probability density

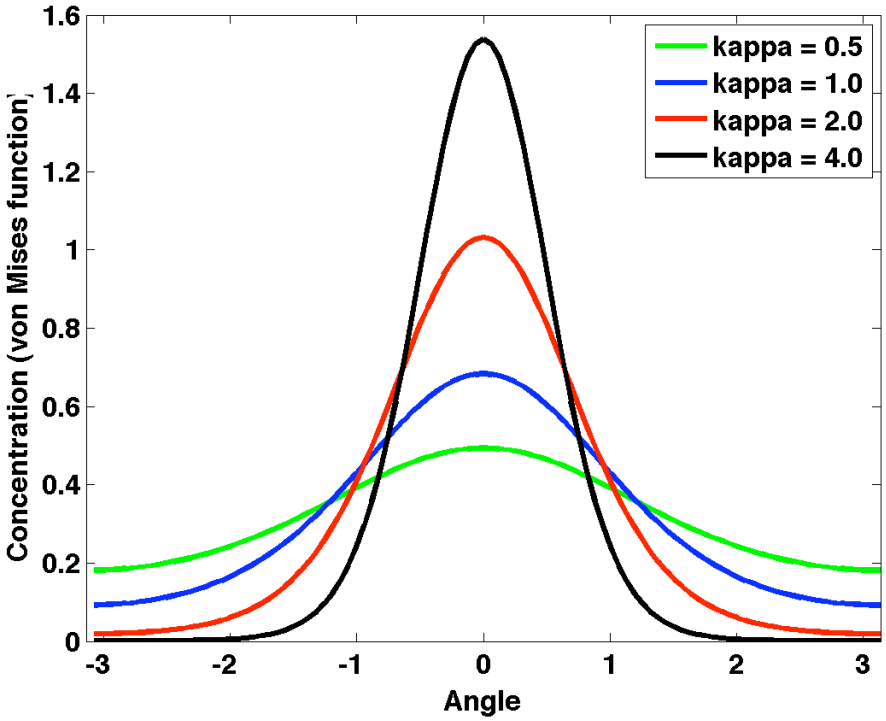

Figure 9: Illustration of von Mises functions, $\rho(\theta|0,\kappa) = \exp[\kappa\cos(\theta)]/\left(2\pi I_0(\kappa)\right)$, with various concentration parameters κ.

function for the angle θ is given by:

$$\rho(\theta|\mu,\kappa) = \frac{\exp[\kappa\cos(\theta-\mu)]}{2\pi I_0(\kappa)} \tag{2.6.1}$$

where I_0 is the modified Bessel function of order 0. The parameter μ can be thought of mean of the distribution. In our case, μ is assumed to be the angle where gradient source is placed. The parameter κ is analogous to $1/\sigma^2$, or the inverse of the variance in a normal distribution. Figure 9 shows the various parameter κ of *von Mises distribution.*

Assume that the distribution of A (or B_m) defines a preferred direction $\bar{\theta}$ and preferred resultant length $\overrightarrow{R}$. If $N(\theta)$ is the number of molecules at θ, the mean angle $\bar{\theta}$ can be calculated by:

$$\overrightarrow{R} = \sum_{\theta} N(\theta) e^{i\theta} = \bar{R} e^{i\bar{\theta}} \tag{2.6.2}$$

Here, we call R the mean resultant length. It is a measure of concentration of a data set and $\bar{\theta}$ is the mean direction

2.7 Amplification

Amplification is a natural quantity for describing the response of a linear signaling system. To discuss "amplification" in a gradient sensing pathway requires some kind of generalization of the usual linear concept.

In the linear setting, imagine we have a random variable $x \sim \mathcal{N}(0, \sigma_x^2)$ which is the "input" to a signaling system. Suppose the output is $y = \alpha x + z$, where α is a positive constant and $z \sim \mathcal{N}(0, \sigma_z^2)$ is the "noise" (independent of x) added to the signal. The output has variance

$$\sigma_y^2 = \alpha^2 \sigma_x^2 + \sigma_z^2 \tag{2.7.1}$$

The mutual information of x and y, which quantifies how much "information" observing y gives you about x, involves the famous signal-to-noise ratio [3]

$$MI(x, y) = \frac{1}{2} \log \left(\frac{\alpha^2 \sigma_x^2 + \sigma_z^2}{\sigma_x^2} \right) = \frac{1}{2} \log \left(\alpha^2 + \frac{\sigma_z^2}{\sigma_x^2} \right). \tag{2.7.2}$$

For an amplitude modulated signal (in the time domain) the input would be a sum of sinusoids of different frequencies ν and the output would have different amplification for different frequencies, i.e. we would have $\alpha(\nu)$. For a variable that is confined to the circle – such as the estimated gradient direction – there are several distributions to choose from. The von Mises distribution provides a natural choice, which interpolates between weak (linear) amplification and strong (nonlinear) concentration of the response. When the concentration parameter $\kappa \ll 1$, we can interpret κ as the

amplitude of the first Fourier component of the (weak, linear) response:

$$e^{\kappa\cos(\theta)} \approx 1 + \kappa\cos(\theta) + O(\kappa^2), \kappa \ll 1. \tag{2.7.3}$$

When $\kappa \gg 1$, we can interpret κ as analogous to the reciprocal variance of a similarly distributed Gaussian near $\theta \approx 0$:

$$e^{\kappa\cos(\theta)} \approx \exp\left[\kappa\left(1 - \frac{\theta^2}{2} + O(\theta^4)\right)\right], \kappa \gg \theta. \tag{2.7.4}$$

If the "input" corresponds to a distribution with concentration κ_{in} and the "output" corresponds to a distribution with concentration κ_{out}, it is natural to define the amplification as

$$\alpha = \frac{\kappa_{out}}{\kappa_{in}} \tag{2.7.5}$$

Figure 11 illustrates the von Mises distribution for different values of κ, and Figure 10 illustrates the input/output plot for a system with different amplification ratios, assuming the input has distribution corresponding to ε or κ_{in} in the von Mises distribution's sense. Comparing this figure to Figure 1 from Janetopoulos *et al* [12], we have a very substantial amplification. The mean slope is about 4.6 which is higher than the polynomial fit slope (red line). In addition, we have an *appropriate* scatter of values in the vertical direction due to stochasticity.

2.8 Variance Growth

Let $\varphi(t) = [x(t), y(t)]^T$ be the random variable representing the position of the particle at time t, given that it started at i at time $t = 0$. Let $\varphi_i(t) = [x_i, y_i]^T$ be the location of the i^{th} node. The probability $p_j(t)$ of being at node j after starting at node i at time zero is given by the matrix exponential solution of equation 2.3.1, namely $(\exp[Qt])_{ji}$. Therefore the variance of the location of a particle moving randomly on

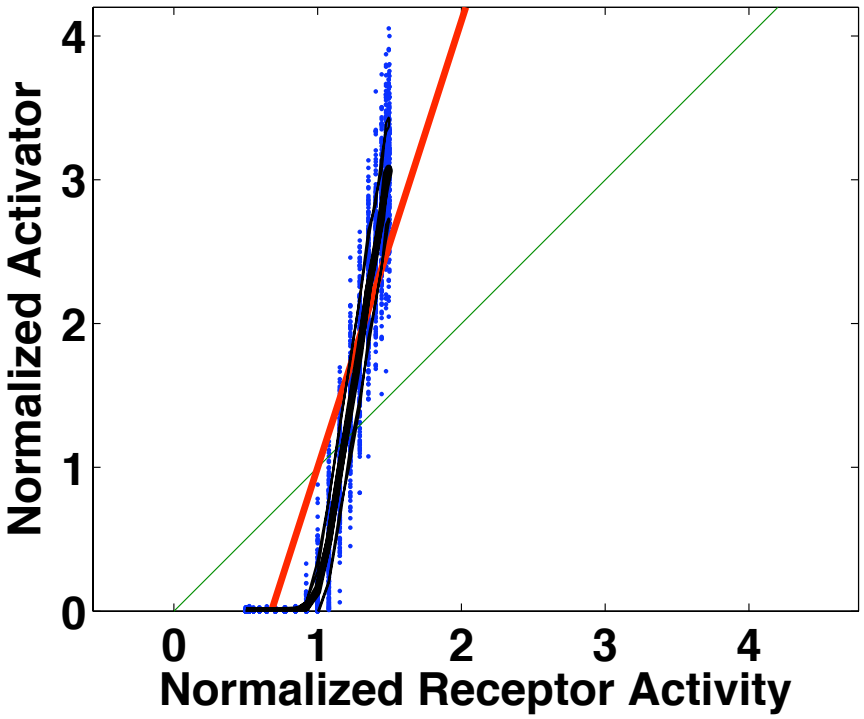

Figure 10: Illustration of amplification ratio of the input activated receptor with $\varepsilon = 0.5$ and $S_0 = 4000$ # mol. Stochastic simulation results.

the graph is (for small times t)

$$
\begin{aligned}
\mathbb{V}[\varphi(t)] &= \mathbb{E}[(\bar{x}(t) - x(t))^2 + (\bar{y}(t) - y(t))^2] \\
&= \sum_j ||\bar{\varphi} - \varphi_j||^2 \left(e^{Qt}\right)_{ji} \\
&= \sum_j \left|\left| \sum_k \left(\exp[Qt]\right)_{ki} \varphi_k - \varphi_j \right|\right|^2 \left(e^{Qt}\right)_{ji} \\
&= \sum_j \left|\left| \sum_k \left(\delta_{ki} + Q_{ki}t + O(t^2)\right) \varphi_k - \varphi_j \right|\right|^2 \left(e^{Qt}\right)_{ji} \\
&= \sum_j \left\{ ||\varphi_i - \varphi_j||^2 + 2t \left((\varphi_i - \varphi_j) \cdot \sum_k \varphi_k Q_{ki} \right) + O(t^2) \right\} \left(e^{Qt}\right)_{ji}.
\end{aligned}
$$

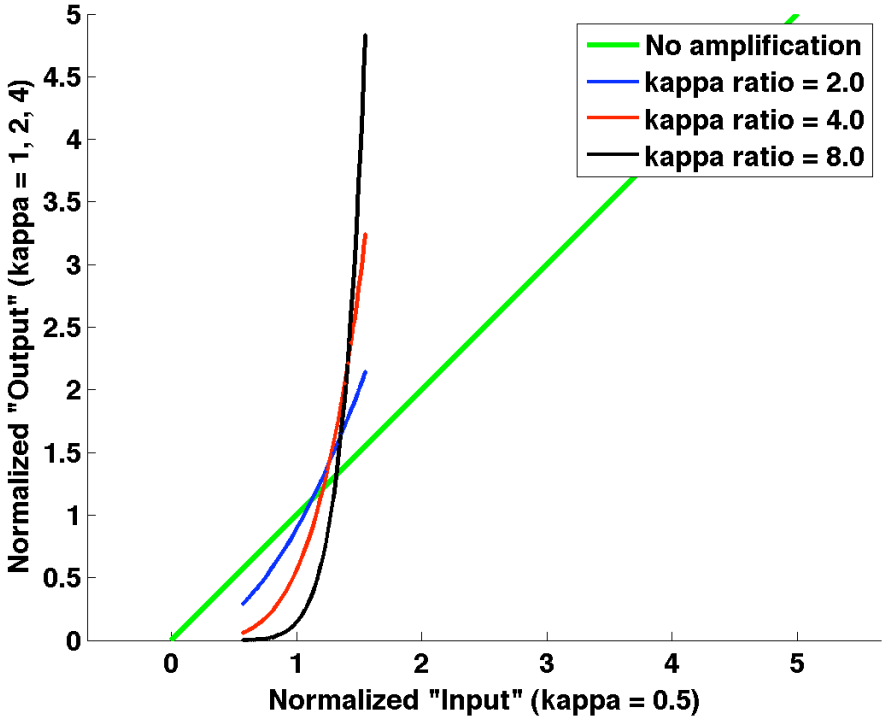

Figure 11: Illustration of amplification ratio defined by the ratio between $\kappa_{input}/\kappa_{output}$ with various values of κ, based on von Mises distribution idealizations.

We can differentiate this expression to obtain the rate of increase of the variance given a delta function initial condition at node i.

$$\begin{aligned} d\mathbb{V}[\varphi(t)]/dt &= \sum_j \left\{ \left(||\varphi_i - \varphi_j||^2 + 2t \left((\varphi_i - \varphi_j) \cdot \sum_k \varphi_k Q_{ki} \right) \right) \left(Q e^{Qt} \right)_{ji} \right. \\ &\quad \left. + 2 \left((\varphi_i - \varphi_j) \cdot \sum_k \varphi_k Q_{ki} \right) \left(e^{Qt} \right)_{ji} \right\} + O(t). \end{aligned} \tag{2.8.1}$$

Evaluating this equation at $t = 0$ we obtain the *initial* rate of increase of the variance from starting node (i), which is

$$\frac{d\mathbb{V}[\varphi(t)]}{dt}|_{t=0} = \sum_{j=1}^{n} ||\varphi_i - \varphi_j||^2 Q_{ji}. \tag{2.8.2}$$

If the rates of growth of the variance are tightly clustered around a given value, that value can be used to determine the effective diffusion constant associated with Q. By

rescaling Q we can then implement a diffusion simulation with a diffusion constant of our choice.

Table 1: Table of parameters and variables specified by Levine *et al.* [18]

symbols	parameters	values and unites
r	the cellular radius	5 μm
D	the diffusion constant	10 μm^2/s
k_a	the rate constant for the reaction $S \rightarrow A + B + S$	1 s^{-1}
k_b	the rate constant for $B \rightarrow B_m$	3 $\mu m/s$
k_{-a}	the rate constant for $A \rightarrow \phi$	0.2 s^{-1}
k_{-b}	the rate constant for $B_m \rightarrow \phi$	0.2 s^{-1}

Table 2: Table of the remaining parameters and variables used in simulation.

symbols	parameters	values and units
dt	the time step size	0.0002 s
S_0	the initial activated receptors	4000 $\#mol/node$
A_0	the number of A at steady state	19.99 $\#mol/node$
B_0	the number of B at steady state	1333.33 $\#mol/node$
$B_{m,0}$	the number of Bm at steady state	19.99 $\#mol/node$
Θ	the true gradient direction	π
θ	the direction that the cell senses	$0 < \theta < 2\pi$
ε	the relative gradient constant	varied
k_i	the reaction rate: $A + B_m \rightarrow (A \,.\, B_m)$	10 $\mu m/\ s \,.\, \#mol$
`nvtxext`	the number of boundary nodes	40 nodes
`nvtx`	the number of nodes	216 nodes
`ntri`	the number of triangles	390 triangles
v_i	the volume associated with node i	varied μm^2
V	the total volume of the cell	78.2172 μm^2
m_i	the number of molecule at node i	varied $\#mol$
c_i	the concentration of particles at node i	varied $\#mol/m^2$
M	the total number of molecule	varied $\#mol$

3 Results

The main purpose of this simulation is to implement a stochastic version of the balanced inactivation model due to Levine *et al.* [18] in a two dimensional geometry and validate the model by comparing to experimental results. The steady state response to stimulation with a spatially uniform concentration of molecule S was calculated by solving the deterministic point model of the system of equations (1.4.1)-(1.4.4). We used the same input S_0 for the stochastic model. As time passed 0.1s, the stochastic elements A, B and B_m, approached their steady states but fluctuated around them. The result of comparing the plot between the deterministic point model and the stochastic model paused at $t = 0.2$ s is shown in Figure 12. This convergence was analyzed further for the stochastic models with various input gradients.

The temporal evolution of the total mass (number of molecules) for each component is presented in Figures 13, 14 and 15 for stimulation with a uniform signal ($\varepsilon = 0$). The total number of A (Figure 13) fluctuates between 500 to 700 molecules for the stochastic simulation (blue line), whereas the deterministic result shows constant mass equal 800 molecules (red line). This mismatch is presumably due to the noise effect in molecular reactions. Similarly, the total number of Bm in the stochastic simulation (Figure 15, blue line) is slightly less than the result from the corresponding determinstic model (same figure, red line). We also note that the total numbers for both A and Bm at the very beginning of the simulation ($t < 0.05s$) are dramatically higher than those for the deterministic simulation. Apparently the spatially uniform steady state values for the numbers of A and Bm are not terribly precise approximations of the means of the distributions of the same molecules under the stochastic simulation. Analysis of the transient from the initial conditions and the approach to the equilibrium distribution are reserved for future work. Significantly, however, the total number of B (Figure 14) shows only an approximately 0.3% discrepancy between the two simulation platforms. This result suggests that the scaled Markov transition matrix may provide an acceptable substitute for the FEM for solution of

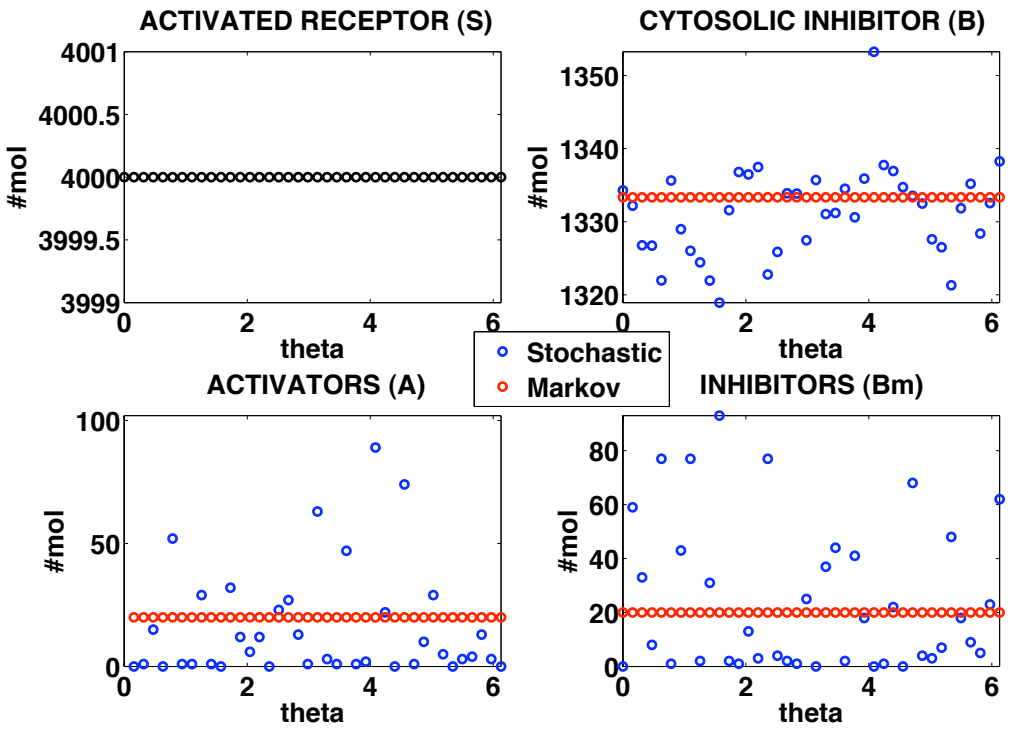

Figure 12: Simulation of the stochastic model (blue circles) and the deterministic Markov transition model (red circles) with uniform stimulation (no gradient), $S_0 = 4000$ $\#mol/node$ and $\varepsilon = 0$.

the diffusion problem for this system.

Comparing the two models, we also applied the stimulus S with various gradients. Figure 16 shows the result of using a fractional gradient $\varepsilon = 0.5$. In Figure 16[C] and 16[D], the results of the expected Markov-transition model agree well with the results of the stochastic model. Figure 16[B] showed a discrepancy ($< 10\%$) between the red and blue curves representing, respectively, the cytosolic distribution of B in the deterministic and stochastic models. Presumably this discrepancy occurred due to differences in implementation of the algorithms representing diffusion. Determining whether the finite element approach or the Markov transition matrix based approach gives a more accurate representation of diffusion for this system remains a problem for future work. However, the discrepancy in B does not appear to affect the distributions of A and Bm, which are used to define the leading edge of the cell. The B molecules in the plot are the number of B molecules located at each node on the membrane. The

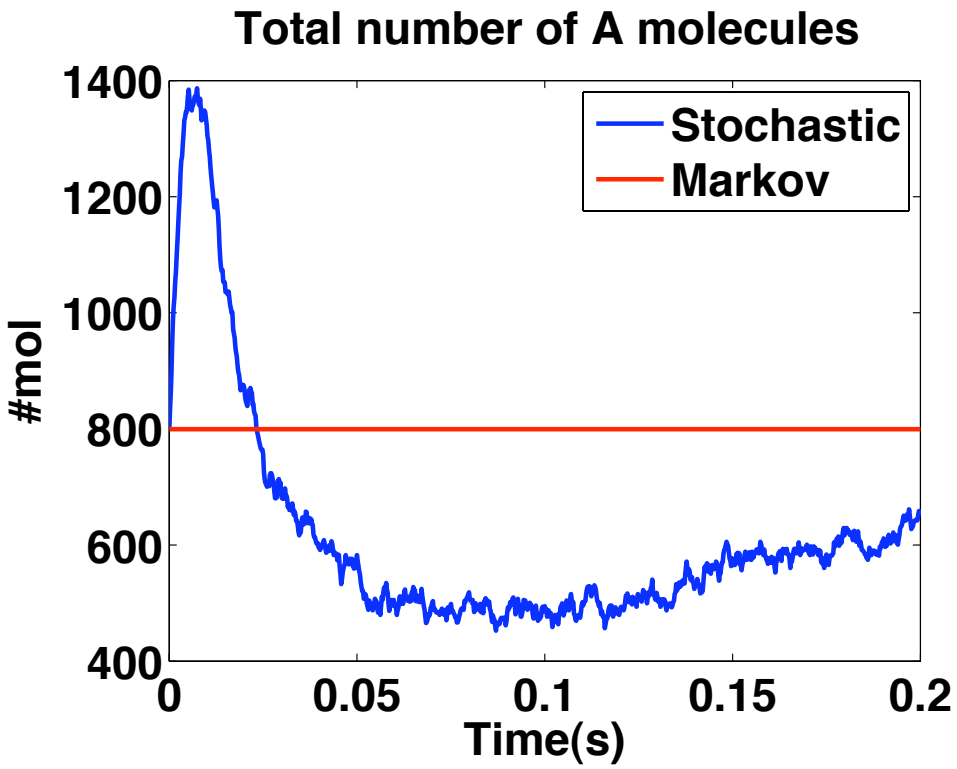

Figure 13: The total number of molecules A bound to the membrane during the simulation. Blue line: stochastic simulation. Red line: determinstic model.

molecules B in the FEM method were dispersed faster than in the expected Markov-transition method. Hence, the collected data at the boundary node was different. Considering both red and blue graphs in Figure 16[B], we knew that the stochastic B element in blue graph tends to have higher diffusion rate than the expected Markov-transition diffusion. Besides the stochasticity in reactions involving B, this error could partly be the effect of scaling the matrix Q to match the diffusion constant.

The predicted direction of motion of the cell is obtained by vector averaging as described above. Figure 16 shows the evolution in time of the inferred gradient direction vector obtained by vector averaging. The deterministic process (red line) always indicates the true direction (π radians) exactly, while the stochastic direction drifts around it. Detailed analysis of this diffusion/drift process on the circle is set aside for future work. In general, we may observe that the direction inferred by the model cell in the stochastic simulation converged to the desired value $\bar{\theta} = \pi$ with only

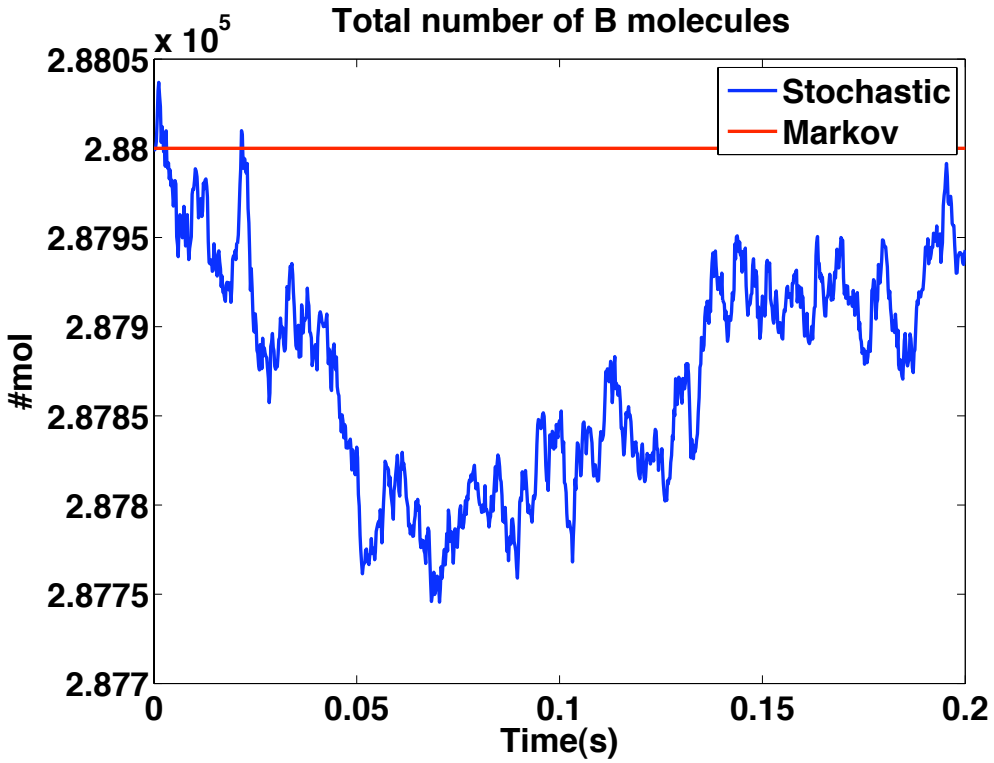

Figure 14: The total number of molecules B in the cytosol during the simulation. Blue line: stochastic simulation. Red line: determinstic model.

a little fluctuation.

Comparing the two models, we also input the S with some gradients. Figure 16 shows the result of when we used a relative gradient constant $\varepsilon = 0.5$. In Figure 16[bottom-left] and Figure 16[bottom-right], the results of expected Markov-transition model agree well with the results of stochastic model. Figure 16[top-right] showed discrepancy ($< 10\%$) between red and blue curves. Presumably this discrepancy occurred due to differences in implementation of the algorithms representing diffusion. Determining whether the finite element approach or the Markov transition matrix based approach gives a more accurate representation of diffusion for this system remains a problem for future work. However, the discrepancy in B does not affect the proportion of A and Bm, which are used to define leading edge of the cell. The B molecules in the plot are the number of B molecules located at each node on the membrane. The molecules B in the FEM method were dispersed faster than in

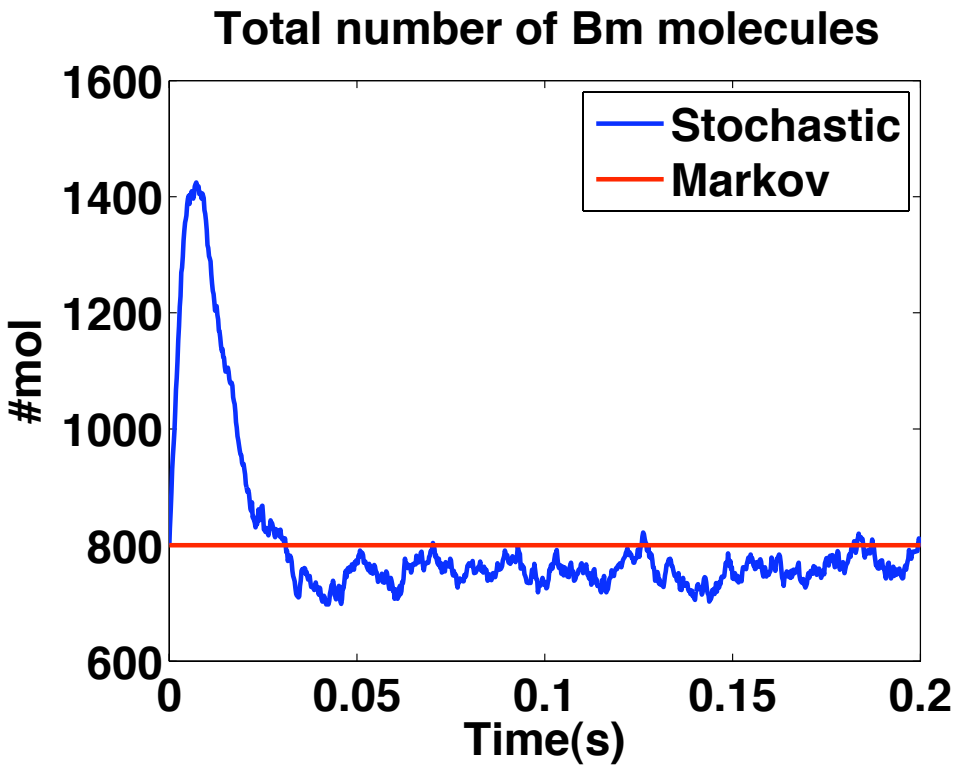

Figure 15: The total number of molecules B bound to the membrane during the simulation. Blue line: stochastic simulation. Red line: determinstic model.

the expected Markov-transition method. Hence, the collected data at the boundary node was different. Considering both red and blue graphs in Figure 16[top-right], we knew that the stochastic B element in blue graph tends to have higher diffusion rate than the expected Markov-transition diffusion. Besides the stochasticity in reactions involving B, this error could partly be the effect of scaling the matrix Q to match the diffusion constant.

We determined the inferred gradient direction in terms of the vector averaged location angle for the population of A molecules, as described in Methods. Figure 16(blue line) shows the mean angle plot of the stochastic and deterministic models. After a brief initial transient the deterministic model's estimated direction was constant at the correct value ($\bar{\theta} = \pi$). The stochastic model's estimate responded to the large gradient (50% gradient) by converging to approximately the same value, with little fluctuation. The fluctuation about the mean appears qualitatively to resemble

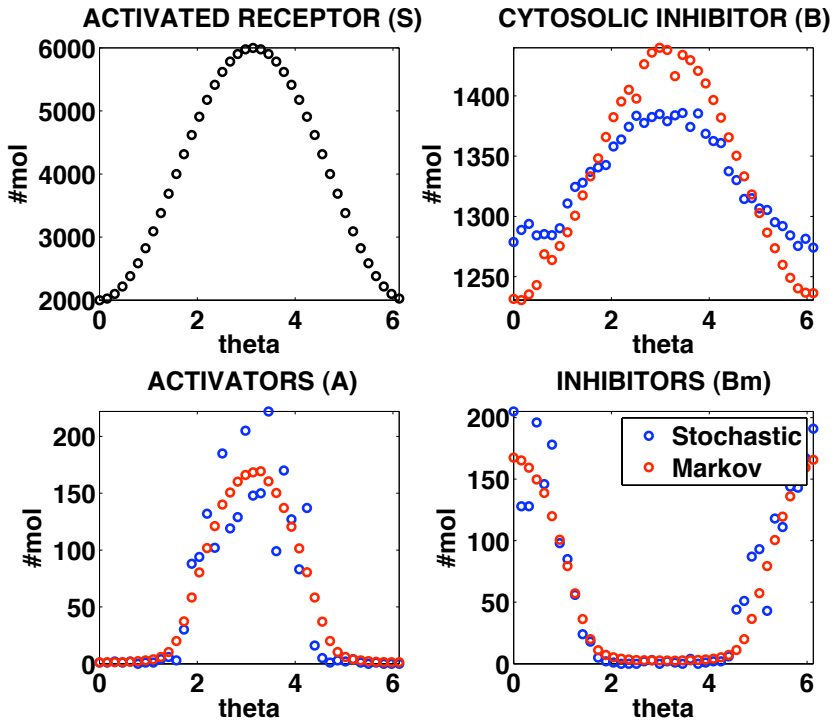

Figure 16: Simulation of the stochastic model (blue circles) and the deterministic Markov transition model (red circles) with stimulation by a large (50%) fractional gradient, $S_0 = 4000$ $\#mol/node$ and $\varepsilon = 0.5$. Note that despite the discrepancy between cytosolic inhibitor levels (top right panel), the activator and membrane-bound inhibitor distributions show good agreement (lower panels).

an Ornstein-Uhlenbeck process (a correlated Gaussian process with decaying mean) except on the circle instead of on the line. Analysis of these fluctuations remains for future work.

In order to verify that our stochastic model gives results consistent with biological experiments, we performed stochastic simulations for 100 different sets of random numbers using a binomial and a possion random generator provided by MATLAB and values of the fractional gradient ε ranging from 0.006 to 1.

Next we calculated amplification ratios using the formula (2.7.5). The results for the simulation of the expected Markov-transition model and stochastic model are shown in Figure 18 and Figure 19 respectively. With shallow gradients (<5 %), the amplification of activator molecules (A) for stochastic model simulation varies

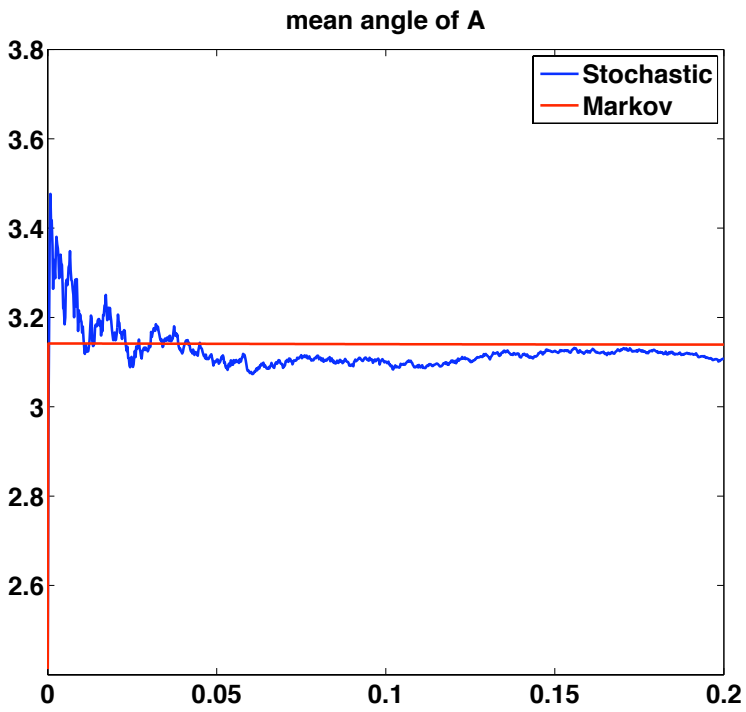

Figure 17: The evolution of mean angle from the stochastic model and the Markov transition model with same given $S_0 = 4000$ $\#mol/node$ and fractional gradient constant $\varepsilon = 0.5$.

between 17 and 24, which is the same range as for the Markov transition model simulation. However, the amplification of the stochastic model fluctuates greatly at shallow gradients. As shown in Figures 21 22, the amplification ratios at shallower gradients for both A and Bm have larger standard deviations. With high gradients ($\approx$ $>$ 50 %), the amplification of A and Bm for stochastic model and Markov transition model are about the same. From this result, the input signals got amplified at a very low $\approx$1 % of gradient across the cell. The amplification ratios imply that at shallow gradients ($\approx$ 1 - 5 %) the output signals get amplified at nearly constant ratios. However, increasing steepness of the gradient signal input makes the amplification ratio decrease once the output signal has reached a point at which nonlinear saturation occurs. For further discussion of this point, please see Section 4.

This observation is consistent with the fact that higher gradients makes stronger signals and noise has less effect to the overall results. On the other hand, the am-

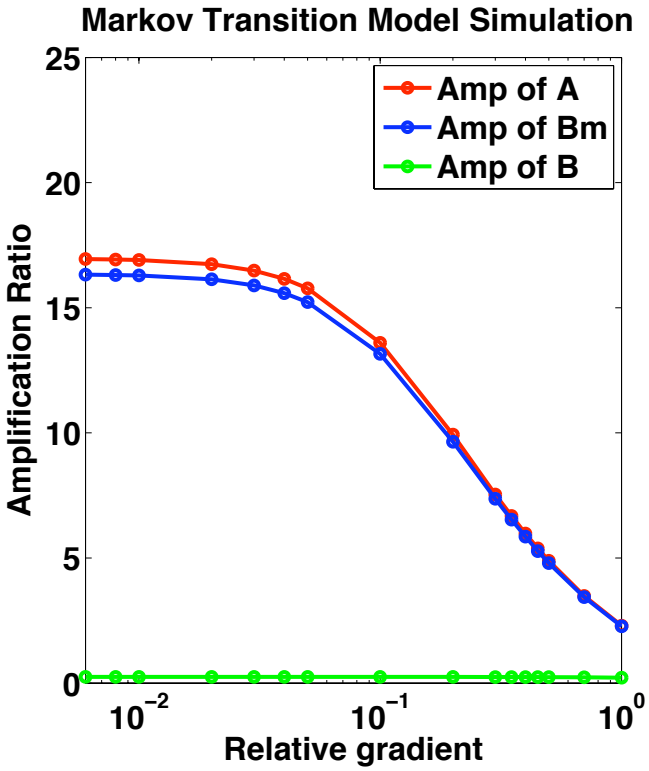

Figure 18: Illustration of amplification ratios defined by the ratio between κ_{in}/κ_{out} for the Markov-transiton model with various fractional gradients (ε).

plification of B for the stochastic model behaves like the amplification of B for the determinstic model independently of the size of the input signal gradient. This is due to the very high diffusion constant ($D = 10\mu m^2/s$). It makes the B molecules spread quickly enough so that their angular distribution is approximately linear. The amplification of B is essentially passive. It reflects the input directly, but is not significantly enhanced by the nonlinear $A : Bm$ interactions occurring on the membrane. Consequently, the amplification of B for both models are approximately constant, and do not exceed unity. In conclusion, the behaviors of both A and Bm are significant in terms of cellular response to the extracellular signal. The output signals A and Bm get amplified at nearly constant ratios at shallow gradient ($\approx$ 1 - 5 %). However, increasing steepness of the input gradient makes the amplification ratios decrease once the input signal has reached its saturation point.

Finally we compared this simulation result to experimental results shown in Fig-

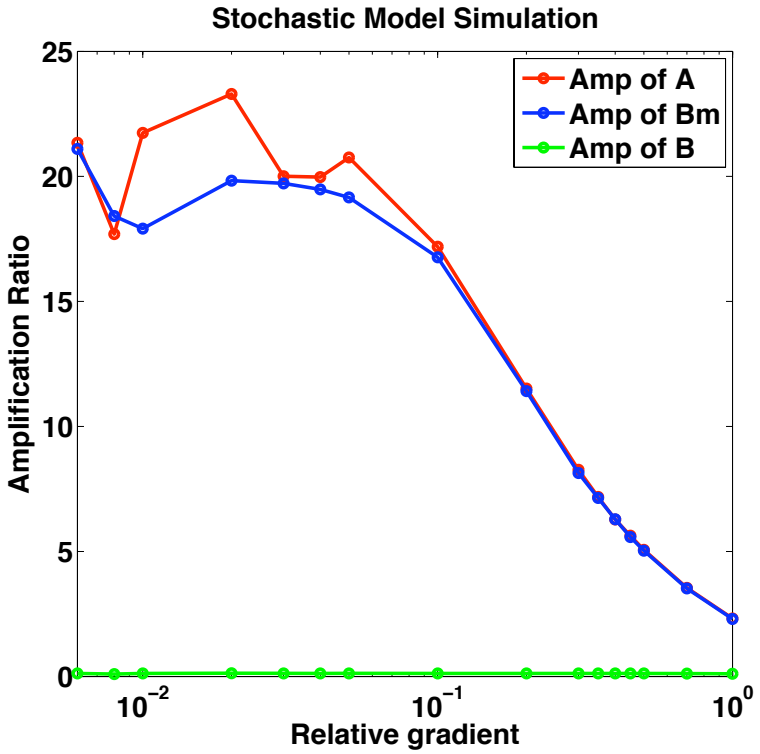

Figure 19: Illustration of amplification ratios defined by the ratio between κ_{in}/κ_{out} for the stochastic model with various fractional gradients (ε).

ure 20 from Janetopoulos *et al.* [12]. The simulation result shows that the amplification of A is higher than the amplification of Bm. This agrees with the result from Janetopoulos *et al.* [12] if molecule A is correlated with PI3K which enhances actin polymerization process and inversely correlated with PTEN.

4 Discussion and Conclusion

In order to validate the simulation results, we compared them with experimental results. Although the three major pathway components studied by Janetopoulos *et al.*, PH-domain protein, PI3K and PTEN, were not measured directly, the investigators fluorescently tagged the components and measured the intensity of fluorescence which varies monotonically with the concentration of PH-domain protein, PI3K and PTEN [12]. We proposed the stochastic simulation platform to quantitatively record

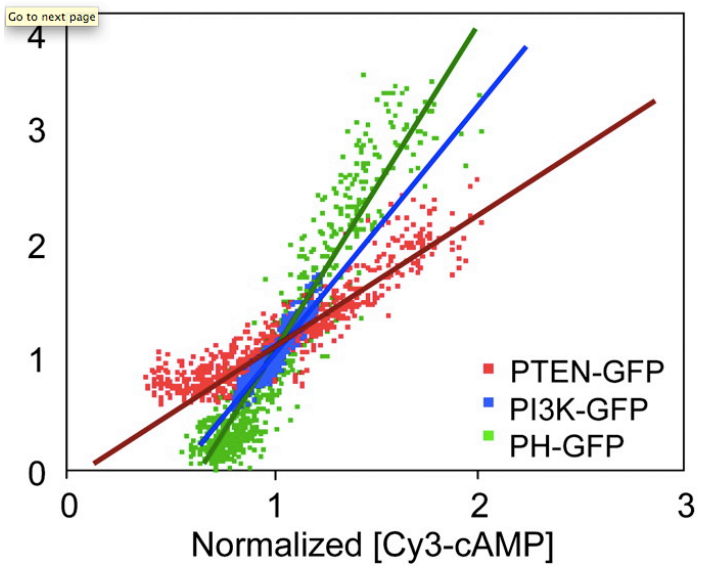

Figure 20: Experimental data from Janetopoulos *et al.* [12] showing the relative degree of amplification of gradient signaling pathway components PI3K (activator), $PI(3,4,5)P_3$ (readout signal), and the inverse of PTEN (inhibitor).

the concentration of A, B and Bm spatially and temporally. In the balanced inactivation model [18], the abstract components, A, B and Bm could correspond to heterotrimetric G protein subunits [18]. Levine *et al.* mentioned that G_α could take the role of activator in the downstream pathway for PH-domain protein localization, whereas $G_{\beta\gamma}$ may be involved in the pathway that localizes other proteins at the back of the cell. The comparison between experimental results and simulation results was considered in qualitative rather than quantitative terms. That is, our abstract activator A could be correlated to the level of PH-domain protein or PI3K, and the inhibitor Bm could be correlated to the level of PTEN. The applied signal S corresponds to the extracellular concentration of chemoattractant applied experimentally, which forms a gradient directed towards the source pipette containing the cAMP analog. (In this project we neglected the saturation of membrane bound receptors in the presence of large concentrations of cAMP. While Levine *et al.* make the same approximation, it should be straightforward to relax it in future work.) From this perspective, we concluded that our simulation results were consistent with experimental observations. The amplification of A is slightly higher than the amplification

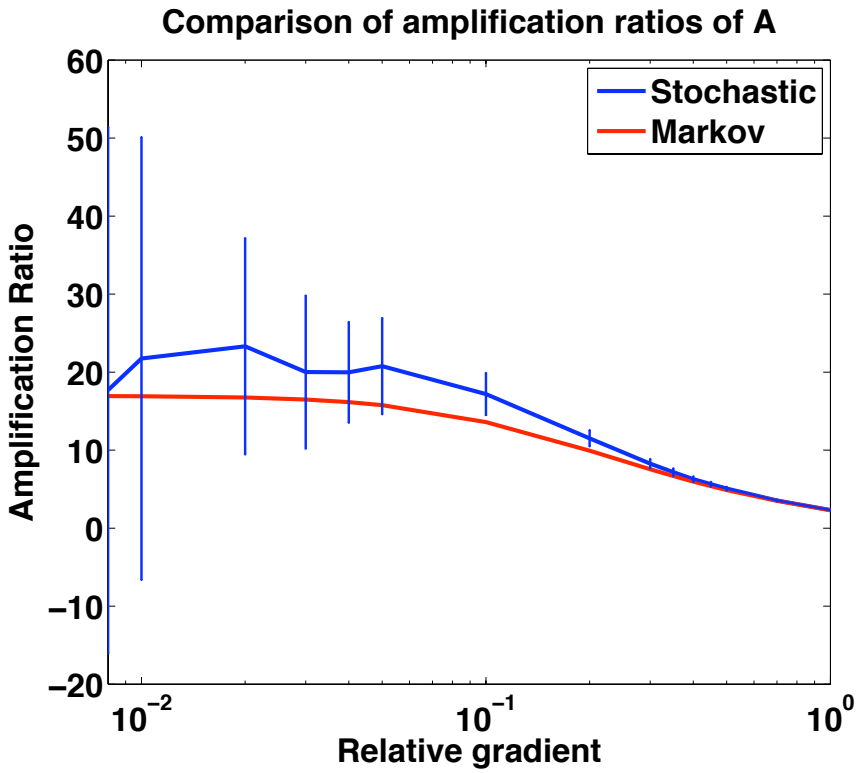

Figure 21: Comparison of amplification for molecule A measured as the ratio of von Mises concentration parameters κ_A/κ_S for the deterministic (red) and stochastic (blue) simulations, as a function of relative gradient ε. Vertical bars denote standard error.

of Bm. When a relative gradient $\approx$ 50 % was applied, we obtained amplification ratio ≈ 5. This amplification ratio matches the amplification result defined by the ratio between the normalized PH-GFP and the normalized Cy3-cAMP, equal 7.1 ± 3.5 [12]. When the gradient has reached its saturation point, the amplification ratio would decrease toward some lower bound. In our case, our lower bound was computed when simulating results with $\varepsilon = 1$. Figure 18 reveals the possibility of finding the lower bound. Janetopoulos *et al.* experimentally showed that the latrunculin-treated cell has less amplification than the motile cell [12]. Since morphology of the cell affects amplification, the very high gradient would increase in the signal amplification if the cell elongates, making the leading edge contains more receptors, and lowering the number of receptors of the tail [22]. This phenomenon would tend to enhance amplification ratio. However, our simulation platform has not been implemented for

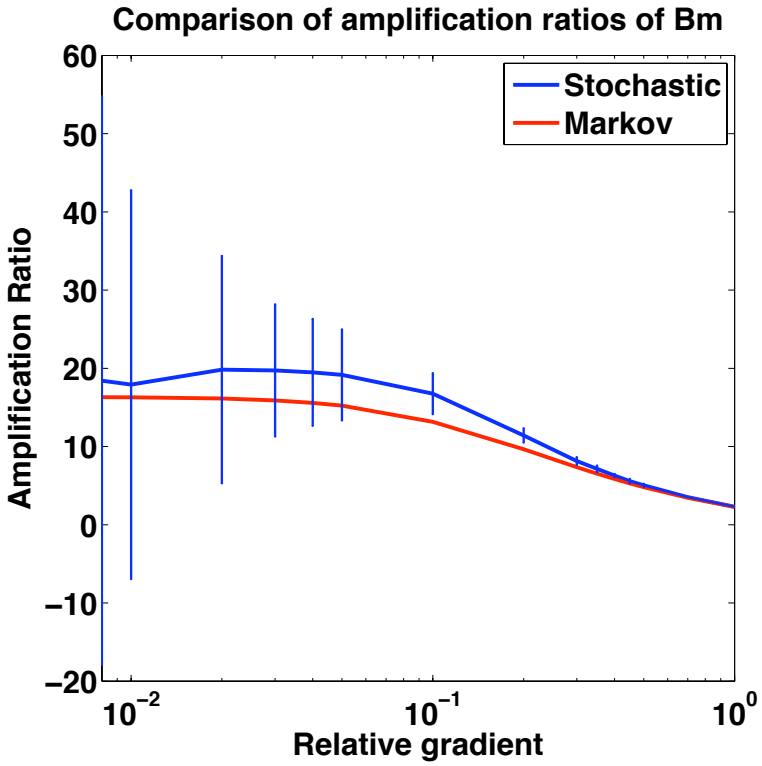

Figure 22: Comparison of amplification for molecule Bm measured as the ratio of von Mises concentration parameters κ_{Bm}/κ_S for the deterministic (red) and stochastic (blue) simulations, as a function of relative gradient ε. Vertical bars denote standard error.

temporal change in cell geometry. Our model cell's circular geometry limits the absolute concentration difference between front and back in a given absolute gradient. Therefore, the simulation results show decreasing amplification ratio as gradient increases. As we have seen in the simulations, the concentrations of A and Bm at time 0.2s (beyond equilibrium) with gradient equal to 50 % (Figure 16) showed that the molecules of A and Bm are very concentrated around π. This concentration of A (resp. Bm) at the leading edge (resp. the rear) of the cell forces the concentration of A (resp. Bm) close to zero at the opposite side of the cell. Figure 23 shows how different gradients affect the corresponding A and Bm distribution at steady state. This figure confirms that the system has a saturation effect. As the gradient increases, the number of molecules A at the trailing edge are close to zero. Because the stochastic simulation represents the numbers of molecules as integers, most of the nodes at the

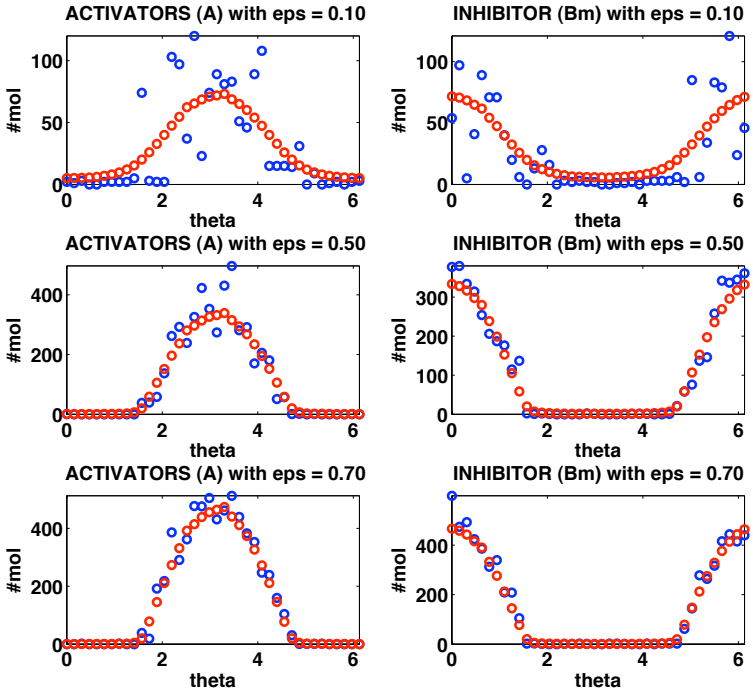

Figure 23: Plots of concentrations of A (left column) and Bm (right column) at time $t = 0.2s$ for different input gradients, $\varepsilon = 0.10$, 0.50 and 0.70. Blue circles: stochastic simulation. Red circles: deterministic simulation. Note the saturation of the response for large gradients.

back of the cell contain *exactly* zero molecules of A, while most nodes at the front contain *exactly* zero molecules of Bm. Because the number of A or Bm cannot drop below zero at any node, it becomes more and more difficult for the cell to sharpen the internal gradient of A or Bm further in the balanced inactivation model. The concentration of A responding to the gradient appears only at the leading edge although we continue to apply constant concentration of extracellular signals. Whether this saturation effect obtains in real cells subjected to higher *versus* lower gradients is an empirical question that could in principle be tested experimentally. In any case, our results agree well with extant biological observations on responses to shallow gradients. For gradient ($< 2\%$), the cell is able to create large internal asymmetry [10]. Performing stochastic simulation for gradient ($< 1\%$), we obtained the cell with high amplification and well-defined leading edge.

The advantage of using the finite element method (FEM) for the gradient sensing model is its flexibility with respect to cell geometry. Cell populations *in vivo* and *in vitro* show a diversity of shapes. Therefore, triangulation is the most suitable method for partitioning the spatial domain representing the projection of the cell on the plane. In addition, the expected Markov-transition method, which is deterministic, needs to be compared with another deterministic method in order to justify its transition matrix. As described, the diffusion problem of B molecules was solved in a different way. We employed FEM for stochastic simulation and Markov transition matrix for the expected Markov-transition simulation. This platform was geared toward our future plan. In future work, we would like to include the stochastic effects of diffusion as well as stochastic effects in the chemical reactions. Using a Markov transition matrix lends itself to putting the diffusive and reactive transitions on a common footing, which is a basis for a full multinomial description of the system [16]. In order to resolve the difficulties in reconciling the FEM and Markov descriptions of the diffusion process we plan to study both descriptions for a regular triangular planar lattice, and small perturbations of a regular traingular lattice tiling the entire plane. When a number of particles are placed at the origin and each has six options with specified probabilities, we can apply the multinomial distribution to the movement of the particles.

In this thesis, we have explored the consequences of stochastic chemical reactions for a particular mechanism proposed to account for gradient sensing. In the case of zeroth and first order chemical reactions, the implementation of stochastic transitions in a fixed timestep framework is relatively straightforward. In order to handle second order (biomolecular) reactions we we applied Kurtz' theorem [14] to approximate the stochastic reaction under the assumption that the number of N_A and N_{Bm} were "sufficiently large". If N_A and N_{Bm} are large, the mean number of occurrences of the stochastic reaction $A+Bm \rightarrow A\cdot Bm$ will approach the number given by deterministic mass action reaction kinetics at each node. Obviously, when the number of A or Bm

are driven close to zero by the mutually inhibitory interaction (at the back or front of the cell, respectively), the large number approximation will not apply. It remains to be investigated, in future work, how well the method employed approximates the number of bimolecular reactions $N_{A.Bm}$ in practice. Therefore, we would further analyze the accuracy of this approximation by comparing to direct simulations with Gillespie's "exact" stochastic simulation algorithm [8], which generates correct statistics for a well-mixed biochemical reaction.

We have introduced a semiquantitative treatment of stochastic noise in an intracellular gradient sensing pathway model. Since the chemotactic cell has some downstream pathways that involve interactions among molecules, the fluctuation may cause inaccurate gradient sensing. However, the fluctuation in downstream pathway was attenuated due to the nonlinear amplification of the signal. The signal amplification facilitated the chemotactic cell to detect a very shallow chemoattactant gradient. Further investigations of the effects of noise can be done by incorporating appropriate stochastic effects into the extracellular signal S. Since each extracellular cAMP molecule has a chance to bind to a membrane receptor, we could take the noise effect of the cAMP-binding to the receptor as a binomial distribution. This approach also appears in Van Haastert and Postma [31]. Analysis of noise propagation in detail and the threshold of noise at which the cell can perceive the true direction of gradient will be explored as further extensions of this project.

References

[1] Howard C. Berg and Edward M. Purcell. Physics of chemoreception. *Biophysical Journal*, 20:193, 1977.

[2] Leonard Bosgraaf, Henk Russcher, Janet L. Smith, Deborah Wessels, David R. Soll, and Peter J.M. Van Haastert. A novel cgmp signalling pathway mediating myosin phosphorylation and chemotaxis in dictyostelium. *EMBO J.*, 21(17):4560–4570, September 2002.

[3] T.M. Cover and J.A. Thomas. *Elements of Information Theory*. John Wiley, New York, 1990.

[4] Peter Devreotes and Chris Janetopoulos. Eukaryotic Chemotaxis: Distinctions between Directional Sensing and Polarization. *J. Biol. Chem.*, 278(23):20445–20448, 2003.

[5] Michael B. Elowitz, Arnold J. Levien, Eric D. Siggia, and Peter S. Swain. Stochastic gene expression in a single cell. *Science*, 297(5584), 2002.

[6] Jonathan Franca-Koh, Yoichiro Kamimura, and Peter Devreotesotes. Navigating signaling networks: chemotaxis in dictyostelium discoideum. *Current Opinion in Genetics and Development*, 16(4):333 – 338, 2006. Pattern formation and developmental mechanisms.

[7] A Gierer and H Meinhardt. A theory of biological pattern formation. *Kybernetik*, 12(1):30–9, Dec 1972.

[8] Daniel T. Gillespie. Exact stochastic simulation of coupled chemical reactions. *The Journal of Physical Chemistry*, 81(25):2340–2361, 1977.

[9] P. A. Iglesias and A. Levchenko. Modeling the cell's guidance system. *Sci STKE*, 2002(148):RE12, 2002.

[10] Pablo A Iglesias and Peter N Devreotes. Navigating through models of chemotaxis. *Current Opinion in Cell Biology*, 20(1):35 – 40, 2008. Cell structure and dynamics.

[11] Robert Insall. Dictyostelium chemotaxis: Fascism through the back door? *Current Biology*, 13(9):R353 – R354, 2003.

[12] C. Janetopoulos, L. Ma, P. N. Devreotes, and P. A. Iglesias. Chemoattractant-induced phosphatidylinositol 3,4,5-trisphosphate accumulation is spatially amplified and adapts, independent of the actin cytoskeleton. *Proc Natl Acad Sci U S A*, 101(24):8951–6, 2004.

[13] Chris Janetopoulos, Tian Jin, and Peter Devreotes. Receptor-mediate activation of heterotrimeric g-proteins in living cells. *Science*, 291:2408–2411, 23 March 2001.

[14] Thomas G. Kurtz. The relationship between stochastic and deterministic models for chemical reactions. *The Journal of Chemical Physics*, 57(7), 1971.

[15] Young W. Kwon and Hyochoong Bang. *The finite element method using MATLAB*. CRC Mechanical Engineering Series. CRC Press, 1996.

[16] Sotiria Lampoudi, Dan T. Gillespie, and Linda R. Petzold. The multinomial simulation algorithm for discrete stochastic simulation of reaction-diffusion systems. *The Journal of Chemical Physics*, 130(9):094104, 2009.

[17] Andre Levchenko and Pablo A. Iglesias. Models of eukaryotic gradient sensing: Application to chemotaxis of amoebae and neutrophils. *Biophysical Journal*, 82:50–63, January 2002.

[18] Herbert Levine, David A. Kessler, and Wouter Jan Rappel. Directional sensing in eukaryotic chemotaxis: A balanced inactivation model. *PNAS*, 103(26):9761–9766, June 27 2006.

[19] Carol L. Manahan, Pablo A. Iglesias, Yu Long, and Peter N. Devreotes. Chemoattractant signaling in dictyostelium discoideum. *Annual Review of Cell and Developmental Biology*, 20(1):223–253, 2004.

[20] Kanti V. Mardia and Peter E. Jupp. *Directional Statistics*. John Wiley & Sons, West Sussex, England, 2000.

[21] Yukihiro Miyanaga, Satomi Matsuoka, Toshio Yanagida, and Masahiro Ueda. Stochastic signal inputs for chemotactic response in dictyostelium cells revealed by single molecule imaging techniques. *Biosystems*, 88(3):251 – 260, 2007.

[22] Matthew David Onsum, Kit Wong, Paul Herzmark, Henry R Bourne, and Adam Paul Arkin. Morphology matters in immune cell chemotaxis: membrane asymmetry affects amplification. *Physical Biology*, 3:190–199, 2006.

[23] Carole A Parent and Peter N. Devreotes. A cell's sense of direction. *Science*, 284:765–770, 30 April 1999.

[24] Marten Postma and Peter J.M. Van Haastert. A diffusion-translocation model for gradient sensing by chemotactic cells. *Biophysical Journal*, 81(3):1314 – 1323, 2001.

[25] Marten Postma, Jeroen Roelofs, Joachim Goedhart, Theodorus W.J. Gadella, Antonie J.W.G. Visser, and Peter J.M. Van Haastert. Uniform cAMP Stimulation of Dictyostelium Cells Induces Localized Patches of Signal Transduction and Pseudopodia. *Mol. Biol. Cell*, 14(12):5019–5027, 2003.

[26] Tatsuo Shibata and Koichi Fujimoto. Noisy signal amplification in ultrasensitive signal transduction. *Proc Natl Acad Sci U S A*, 102(2):331–336, 2005 Jan 11.

[27] Tatsuo Shibata and Masahiro Ueda. Noise generation, amplification and propagation in chemotactic signaling systems of living cells. *Biosystems*, 93(1-2):126–132, Jul-Aug 2008.

[28] Robert T. Tranquillo and Douglas A. Lauffenburger. Stochastic model of leukocyte chemosensory movement. *J Math Biol.*, 25(3):229–62, 1987.

[29] Robert T. Tranquillo, Douglas A. Lauffenburger, and S.H. Zigmond. A stochastic model for leukocyte random motility and chemotaxis based on receptor binding fluctuations. *J Cell Biol*, 106(2):303–9, Feb 1988.

[30] Alan M. Turing. The chemical basis of morphogenesis. *Phil. Trans. Roy. Soc. Lond*, B237:37–72, 1952.

[31] Peter J M van Haastert and Marten Postma. Biased random walk by stochastic fluctuations of chemoattractant-receptor interactions at the lower limit of detection. *Biophys J*, 93(5):1787–1796, Sep 1 2007.